Summer 7-2022

Modeling and Analysis of a 12kW Solar-Wind Hybrid Renewable Energy System

Ekaterina Muravleva
University of Nebraska-Lincoln, emuravleva2@huskers.unl.edu

MODELING AND ANALYSIS OF A 12kW SOLAR-WIND HYBRID RENEWABLE ENERGY SYSTEM

by

Ekaterina Muravleva

A THESIS

Presented to the Faculty of

The Graduate College at the University of Nebraska

In Partial Fulfillment of Requirements

For the Degree of Master of Science

Major: Electrical Engineering

Under the Supervision of Professor Jerry Hudgins

Lincoln, Nebraska

July 2022

MODELING AND ANALYSIS OF A 12kW SOLAR-WIND HYBRID RENEWABLE ENERGY SYSTEM

Ekaterina Muravleva, MS
University of Nebraska, 2022

Advisor: Jerry Hudgins

The increase in rate of depletion of natural resources in the last decade as well as the increased global focus on climate change has made the transition to renewable resources of energy a priority for various countries and organizations across the globe. The sporadic nature of energy generated by photovoltaic systems and wind energy conversion systems has led to an increased utilization of more reliable hybrid renewable energy systems. A combination of both solar and wind energy-based power generations systems reduces the impact of seasonal variation on the amount of power generated and therefore, can be used under varying weather conditions.

This research aimed to design a 12kW hybrid photovoltaic-wind renewable energy system for utility scale implementation. The study provides a detailed description of various components required to create a grid-connected hybrid system. The proposed system constituted a 12.8kW PV array and a 12kW wind turbine, and the input solar and wind data were utilized for the region of Valentine in Nebraska. The selection and/or design procedure of various sub-components such as boost converter, permanent magnet synchronous generator, maximum power point tracking system, converters, etc. were also studied and elucidated in order to provide a detailed understanding of a small power hybrid generation system. The output voltage and power characteristics from the hybrid systems as well as wind and solar systems separately were generated and analyzed. Finally, a cost analysis of the hybrid system was conducted in order to calculate the payback period.

ACKNOWLEDGEMENTS

I would like to express my heartfelt gratitude to my advisor, Dr. Jerry Hudgins, for generously mentoring me all through the path of my graduate studies and advising me during my research. His timely advices have helped me a great extent throughout the course of this research.

I would also like to thank my supervisory committee members, Dr. Sohrab Asgarpoor and Dr. Qing Hui, for graciously serving in my committee, and for all their time and suggestions for improving this research. Additionally, I would like to acknowledge Dr. Jun Wang for his valuable comments and instructive insights into the renewable energy system model design.

I would like to thank my family for their continuous support and for motivating me to believe in myself. I would also like to acknowledge my colleagues, department faculty and staff for making my University of Nebraska experience delightful.

.

LIST OF FIGURES

LIST OF TABLES

LIST OF ACRONYMS

AC	Alternating current
AI	Artificial intelligence
CCM	Continuous conduction mode
CV	Constant voltage
DC	Direct current
DCM	Discontinuous conduction mode
DFIG	Doubly fed induction generator
DOD	Depth of discharge
EMF	Electromotive force
FLC	Fuzzy logic controller
HRES	Hybrid renewable energy system
HSWSO	Hybrid solar-wind system optimization sizing
IEC	International Electrotechnical Commission
INC	Incremental conductance
IRENA	International Renewable Energy Agency
I-V	Current-Voltage
LC	Inductor-Capacitor
LCL	Inductor-Capacitor-Inductor
LPSP	Loss of power supply probability
MPPT	Maximum power point tracking
NREL	National Renewable Energy Laboratory
P&O	Perturb and observe
PD	Proportional-Derivative
PI	Proportional-Integral
PID	Proportional-Integral-Derivative
PMSG	Permanent magnet synchronous generator
PV	Photovoltaic
P-V	Power-Voltage
PWM	Pulse width modulation
RES	Renewable energy source
SCIG	Squirrel-cage induction generator
SOC	State of charge
USD	United States Dollar
VOC	Voltage oriented control
WECS	Wind energy conversion systems
WT	Wind turbine

1. INTRODUCTION

Adoption of environmentally sustainable technologies, energy efficiency improvement, forest conservation, water conservation, energy saving, and promotion and implementation of renewable energy sources are considered some of the most effective methods to address climate change [1]. In addition to mitigating carbon dioxide emission, utilization of renewable energy sources assists in improving the macroeconomic efficiency of economies [1]. Studies have indicated that since 2010, natural resources are being depleted 20% faster that they can be recharged [2]. This makes it vital to increase the pace of transition to renewable resources of energy.

Renewable energy sources (RESs) are increasingly taking a considerable share of global electricity generation with climate change and rapid industrial growth acting as a catalyst for their adoption [3]. The addition of 139 GW of new solar installations and 93 GW of wind power installations led to RESs constituting 29% of global electricity generation in 2020 [4]. This remarkable adoption of RESs, specifically solar and wind energy systems, comes with the drawback of fluctuating energy production due to unpredictable nature of solar and wind resources [5].

Renewable energy systems could either be connected directly to the grid or be designed to operate in a standalone mode, with the latter being used mostly in remote and rural areas which are isolated from the utility grid [6]. The energy generated by a standalone photovoltaic (PV) system is unstable and sporadic because it depends on the weather conditions and time of the day [7]. Since these PV systems can operate only during the day when sun light is in abundance, they either require additional energy storage devices like a battery bank or a secondary source of energy such as a diesel generator. Additionally, standalone wind energy conversion systems (WECS) do not generate usable energy for substantial stretches of the year due to low actual wind speeds as compared to a typical cut-in speed of 3.5-4.5 m/s [8]. To overcome these obstacles, utilization of hybrid renewable energy systems (HRES) is gaining traction since these have been proven to be more reliable than standalone solar or wind energy systems [9].

There are two modes of operation of hybrid PV and WECS: simultaneous and sequential [10]. In simultaneous mode, both wind turbine and PV array generate energy at the same time whereas in sequential mode, the electricity is produced alternatively by the two systems. Utilization of a simultaneous hybrid renewable energy system is

more efficient than using standalone solar or wind energy systems because they allow for the system load to be met in an optimum manner [6, 8].

In additional to seasonal variation, the efficiency of solar cells and wind turbines is another challenge that must be taken into consideration while implementing an HRES. According to National Renewable Energy Laboratory (NREL), depending on the photovoltaic technology, the efficiency of solar cells varies from 13% to 47.1%, with higher efficiency cells mostly used for research purpose and not financially viable (figure 1.1). Similarly, there is a physical limit to the maximum efficiency of a wind turbine, irrespective of its design [11]. The amount of energy generated by a wind turbine depends on the wind speed reduction when it reaches the turbine blade [11]. To achieve 100% efficiency, the wind velocity must reach zero which is not practical, and therefore leads to a maximum efficiency of 59.3% or a power coefficient of 0.593 which is referred to as Betz limit [11].

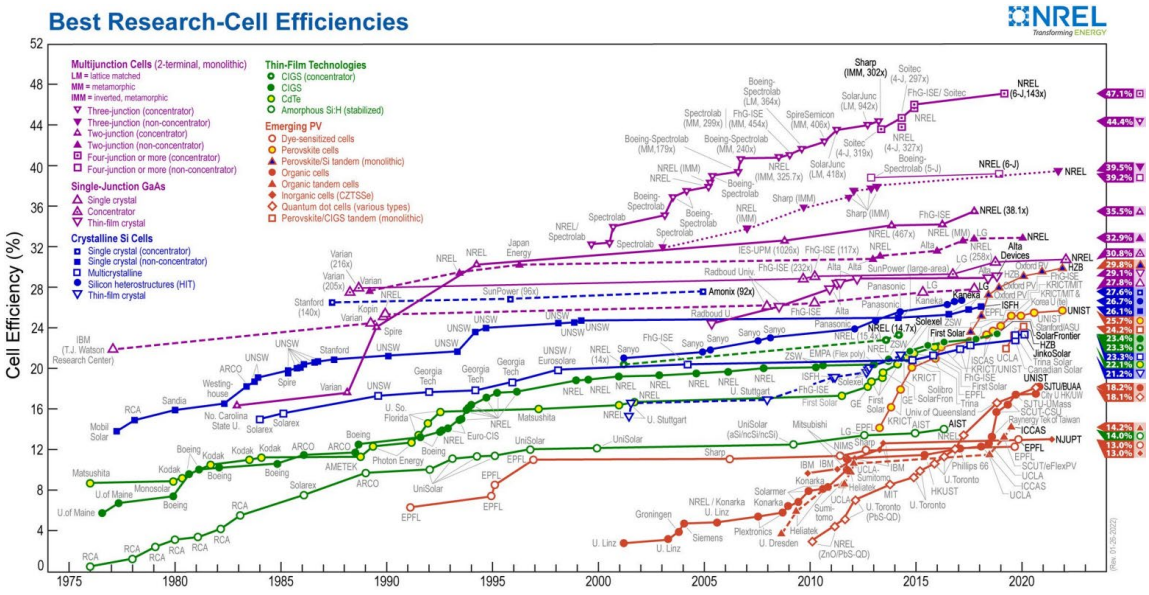

Figure 1.1. Solar cell efficiency for various technologies [12]

Hitaj and Suttles [13] estimated that the electricity consumption was 150kWh per day for wheat farms, 250kWh per day for corn farms, and 806kWh per day for dairy farms. Considering a hybrid system with 40% capacity factor, a 15.6kW system would, therefore, be sufficient to meet the electricity demands of a wheat farm. Similarly, a 26kW system for a corn farm and an 84kW system would suffice for corn and dairy farms respectively. But large wind turbines require higher cut-in speeds to start generating power and larger solar farms require substantial space and capital.

Therefore, an optimum size of a PV-wind hybrid renewable energy system is vital to be able to generate an efficient but affordable system that can be used under varying weather conditions [14].

Hence, this research aims to design a 12kW hybrid PV-wind system that could be utilized to meet the demands of such rural agricultural operations. Furthermore, the specifications of the components used to design the system are enlisted and design criteria explained in order to practically implement the system in regions where it will be environmentally and financially suitable. Several studies have been conducted on hybrid renewable energy systems over the last few years and some of the key aspects studied in literature are briefly discussed in the following subsection.

Literature Review

Multiple researchers have conducted research on standalone PV and wind energy systems. However, these systems come with the drawback of unstable power generation due to weather conditions, as mentioned in the previous section. PV power generation systems are becoming increasingly popular due to solar energy being clean, inexhaustible and pollution-free energy source in addition to the low maintenance, lack of wear and lack of noise of solar array due to absence of moving parts [15]. Molina and Espejo [15] proposed a mathematical model and control scheme for a three-phase grid-connected PV system with a perturb and observe (P&O) incorporated maximum power point tracking (MPPT) mechanism. The proposed model was designed and tested for a small-scale 250W PV system and a comparative analysis of output power with and without MPPT depicted significant reduction in the output power when MPPT was deactivated. Similarly, Chermitti et. al. [16] designed a model for a small-scale 60W PV system, and Ding et. al. [17] designed and validated a 50W PV power generation module. Most of the literature dealing with modeling and testing of solar power generation systems deals with very low output power and therefore, are not suitable for most practical rural applications.

Most of the literature related to WECS presented designs for either high power output turbines in more than 500 kW range or low power output systems of less than 5 kW, both of which are unsuitable for practical rural applications. Behabtu et. al. [18] identified wind speed variation, system operating cost, power quality and power imbalances as major challenges in integrating wind energy into the grid system. The authors suggested installing an energy storage technology in order to overcome the

issue of intermittent power generation in grid connected WECS. A 9MW grid-connected squirrel-cage induction generator (SCIG) and a 9MW grid-connected doubly fed induction generator (DFIG) wind turbine was modeled and simulated using MATLAB/Simulink. The result showed that the output power from the SCIG wind turbine fluctuated for the initial two seconds due to the wind turbine being directly connected to the grid without using power converters. On the other hand, there were no fluctuations in the output power from the DFIG wind turbine because the active and reactive powers were controlled by installing a power converter. Similarly, Saheb-Koussa et. al. [19] developed a model for a 660kW grid-connected wind turbine energy generation system and analyzed the system behavior using hourly wind speed data in Southern Algeria. Mohammadi et. al. [20] designed, simulated and conducted experimental study on 5.5kW small wind turbines, and the performance analysis proved that the power and current fluctuated due to wind turbulence. In order to minimize some of weather fluctuation related drawbacks of standalone PV and wind energy systems, hybrid PV-wind renewable energy systems with MPPT are increasingly being studied and installed globally.

Jian et. al. [21] classified and summarized the system configuration and design of medium and large scale off-grid hybrid power generation systems. The authors thoroughly explained various components of a wind-solar hybrid power generation system including PV system, wind system, battery units, diesel generator, related electrical devices and loads. The author classified HRESs into three types based on busbar forms, with the three classifications being pure AC busbar system, pure DC busbar system and hybrid AC-DC busbar system. The control strategy was identified as the primary challenge in off-grid HRESs and therefore 27 different operation modes were identified and discussed in order to formulate a robust control strategy.

Arribas et. al. [22] pointed out that although IEC-61724 was available as an internationally accepted guideline to monitor the performance of a photovoltaic system, there were no such guidelines available for a hybrid renewable energy system. This research was therefore carried out to create a new tool, based on IEC-61724, for performance monitoring and long-term behavior characterization of a PV-wind HRES. The principal approach was to suggest the parameters necessary to characterize wind generation that primarily affect electrical energy quantities and system performance indicators. The proposed guidelines were applied to a 5kW PV - 7.5kW wind hybrid

system in Soria, Spain and all necessary performance parameters were tabulated for the case study in consideration.

Salameh and Davis [14] investigated into the effectiveness of a grid-connected, residential scale HRES consisting of wind turbines and photovoltaic array. A hybrid renewable energy system consisting of three wind turbines – 1.5kW at 80' above ground level, 500W at 45' above ground level and 300W at 45' above ground level; 2.5kW solar array at 40' above ground level; microprocessor controlled MPPT for PV array; a 24V battery module; and a 4kW inverter connected to utility grid in a conventional 120V AC sub-panel, was installed to study its effectiveness as distributed generation and demand-side management. The researchers found that the larger wind turbine of 1.5kW which was expected to be most effective had a lower capacity factor than the 500W wind turbine. This was because the larger wind turbine required higher cut-in speeds for power generation and had a reduction in its ability to respond to dynamic gusts. The authors further elucidated the economic feasibility and the environmental impact of the system. This research is vital to understand the importance of wind turbine size for an HRES. A very large wind turbine was therefore not utilized in the design of the hybrid system for the current research.

Yang and Zhou [23] developed an optimization model for optimum capacity sizing of various components of a hybrid solar-wind power generation system. The authors employed loss of power supply probability (LPSP) approach to develop an optimal tool for hybrid solar-wind system optimization sizing (HSWSO). LPSP is the probability that a power supply deficit occurs when the hybrid system is incapable of to meet the load demand. The sizing parameters considered were PV system capacity, rated power of wind system, and battery backup capacity in addition to wind turbine height and PV module orientation. In addition to developing the model, the authors carried out a case study to optimize the sizing and operating characteristics of a 1kW hybrid system for a communication system based in China. The results indicated that zero LPSP could only be achieved at 10kW rated power of wind turbine and 270 PV modules for standalone systems with a one-day battery bank storage capacity. Therefore, taking into consideration the literature and electricity requirement for various farm processes, a 12kW hybrid system was proposed under the scope of the current research.

Furthermore, design and analysis of various sub-components to be implemented in standalone or hybrid solar and wind energy systems has been extensively conducted in literature. A vital decision to be taken while designing the proposed system was whether

to implement MPPT or not. Chy and Khaliluzzaman [24] modelled a PV system consisting of a non-inverting buck-boost converter based on MPPT and non-MPPT techniques. The researchers implemented a modified P&O algorithm through a buck-boost converter, the duty cycle of which was automatically controlled using a microcontroller. A comparative analysis of MPPT and non-MPPT schemes was conducted and the results showed that the efficiency of the system was approximately 86% higher with MPPT when compared to non-MPPT system.

Rozi and Salimin [25] designed a standalone PV, standalone wind and a hybrid PV-wind renewable energy system using solar and wind data from Ayer Hitam, Malaysia. The PV system was designed using mathematical equations based on a single diode equivalent circuit and both systems were connected to the dc link for a more stable dc output. The power output was low because the research did not employ an MPPT. Furthermore, the lack of energy storage system was a limitation in the study that was specified as a topic of future research by the authors.

Kumari [26] proposed a hybrid PV-wind system with the primary objective of the study being to tracking the maximum power of the system by using P&O algorithm. The analysis was carried out at various irradiance levels, temperature points and wind speeds. The author concluded that the proposed system was able to meet the electricity demand due to implementation of MPPT. Therefore, it was concluded that a significant amount of power was wasted by not implementing MPPT. Based on the review of literature, MPPT was implemented in the proposed model in order to obtain maximum power from the system at all times.

Finally, DC-DC boost converter is a key component in designing a PV-wind HRES since it converts the variable input voltage due to weather dependence to a constant output voltage which can be connected to the grid and battery through an inverter. Masri and Chan [27] introduced a methodology to design and develop a dc-dc boost converter with constant output voltage. The researchers designed a boost converter operated in continuous conduction mode (CCM) in order to step up a fluctuating input voltage to a constant 24V. The authors elucidated the selection process of electronic switch, inductor, diode and output capacitor. Furthermore, the efficiency of the designed boost converter was tabulated for multiple input voltage, input current and duty cycles.

Research Objectives

Utilizing the design methodology of various sub-components explained in the literature, the study aims to:

1. Model and analyze a grid-connected 12kW PV-wind hybrid renewable energy system.
2. Describe the selection and/or design process of various sub-components implemented in the proposed model.
3. Conduct an economic analysis of the proposed model using the data from the region of Valentine in Nebraska.

The results from the research are meant to provide a better understanding of components required to install a grid connected hybrid PV-wind energy system that can be utilized to perform various farm processes. The complete proposed model and detailed design parameters of all sub-components required to design it are described in the next chapter. Furthermore, the effect of using various components such as PI controllers and MPPT on the generated power and other important parameters is explained along with the description of complete model.

REFERENCES

[1] T. Chien, and J.L. Hu, "Renewable energy: An efficient mechanism to improve GDP," *Energy Policy*, vol. 36, pp. 3045-3052, 2008, doi:10.1016/j.enpol.2008.04.012

[2] R. Hafezi, and M. Alipour, "Renewable energy sources: Traditional and modern age technologies," in *Encyclopedia of the UN Sustainable Development Goals*, 2020, doi:https://doi.org/10.1007/978-3-319-71057-0_18-1

[3] F.R. Alharbi, and D. Csala, "GCC countries' renewable energy penetration and the progress of their energy sector projects," *IEEE Access*, vol. 8, pp. 211986-212002, 2020, doi:10.1109/ACCESS.2020.3039936

[4] REN21 Renewables Now, "Renewables 2021 Global Status Report," 2021. [Online]. Available: https://www.ren21.net/wp-content/uploads/2019/05/GSR2021_Full_Report.pdf

[5] W. Zhou, C. Lou, Z. Li, L. Lu, and H. Yang, "Current status of research on optimum sizing of stand-alone hybrid solar-wind power generation systems," *Applied Energy*, vol. 87, pp. 380-389, 2010, doi:10.1016/j.apenergy.2009.08.012

[6] B. Kanagasakthivel, and D. Devaraj, "Simulation and performance analysis of Solar PV-Wind hybrid energy system using MATLAB/SIMULINK," *2015 International Conference on Computing and Communications Technologies (ICCCT)*, 2015, pp. 99-104, doi:10.1109/ICCCT2.2015.7292727.

[7] A. Aktas, and Y. Kircicek "Solar system characteristics, advantages, and disadvantages," in *Solar Hybrid Systems,* 2021, ch. 1, pp. *1-24*.

[8] M.A. Elhadidy, and S.M. Shaahid, "Promoting applications of hybrid (wind + photovoltaic + diesel + battery) power systems in hot regions," *Renewable Energy*, vol. 29, pp. 517-528, 2003, doi:10.1016/j.renene.2003.08.001

[9] B.D. Vick, and B.A. Neal, "Analysis of off-grid hybrid wind turbine/solar PV water pumping systems," *Solar Energy*, vol. 86, pp. 1197-1207, 2012, doi:10.1016/j.solener.2012.01.012

[10] V. Khare, S. Nema, and P. Baredar, "Solar-wind hybrid renewable energy system: A review," *Renewable and Sustainable Energy Reviews*, vol. 58, pp. 23-33, 2016, doi:http://dx.doi.org/10.1016/j.rser.2015.12.223

[11] P.J. Schubel, and R.J. Crossley, "Wind turbine blade design," *Energies*, vol. 5, pp. 3425-3449, 2012, doi:10.3390/en5093425

[12] National Renewable Energy Laboratory, "Best research-cell efficiency chart," NREL.gov. https://www.nrel.gov/pv/cell-efficiency.html (accessed April 10, 2022)

[13] C. Hitaj, and S. Suttles, "Trends in U.S. agriculture's consumption and production of energy: Renewable power, shale energy, and cellulosic biomass," *USDA Economic Information Bulletin*, vol. 159, 2016

[14] Z. M. Salameh and A. J. Davis, "Case study of a residential-scale hybrid renewable energy power system in an urban setting," *2003 IEEE Power Engineering Society General Meeting (IEEE Cat. No.03CH37491)*, vol. 4, pp. 2320-2322, 2003, doi:10.1109/PES.2003.1270990.

[15] M.G. Molina, and E.J. Espejo, "Modeling and simulation of grid-connected photovoltaic energy conversion systems," *International Journal of Hydrogen Energy*, vol. 39, pp. 8702-8707, 2014, doi:http://dx.doi.org/10.1016/j.ijhydene.2013.12.048

[16] A. Chermitti, O. Boukli-Hacene, A. Meghebbar, N. Bibitriki, and A. Kherous, "Design of a library of components for autonomous photovoltaic system under Matlab/Simulink," *Physics Procedia*, vol. 55, pp. 199-206, 2014, doi:10.1016/j.phpro.2014.07.029

[17] K. Ding, X. Bian, H. Liu and T. Peng, "A MATLAB-Simulink-Based PV Module Model and Its Application Under Conditions of Nonuniform Irradiance," in *IEEE Transactions on Energy Conversion*, vol. 27, no. 4, pp. 864-872, Dec. 2012, doi:10.1109/TEC.2012.2216529.

[18] H.A. Behabtu, T. Coosemans, M. Berecibar, K.A. Fante, A.A. Kebede, J.V. Mierlo, and M. Messagie, "Performance evaluation of grid-connected wind turbine generators," *Energies*, vol. 14, no. 6807, pp. 1-19, 2021, doi:https://doi.org/10.3390/en14206807

[19] D. Saheb-Koussa, M. Haddadi, M. Belhamel, S. Hadji, and S. Nouredine, "Modeling and simulation of the fixed-speed WECS (wind energy

conversion system): Application to the Algerian Sahara area," *Energy*, vol. 35, pp. 4116-4125, 2010, doi:10.1016/j.energy.2010.06.032

[20] E. Mohammadi, R. Fadaeinedjad, and H.R. Naji, "Platform for design, simulation, and experimental evaluation of small wind turbines," *IET Renew. Power Gener.*, vol. 13, no. 9, pp. 1576-1586, 2019, doi:10.1049/iet-rpg.2018.5667

[21] C. Jian, C. Yanbo and Z. Lihua, "Design and research of off-grid wind-solar hybrid power generation systems," *4th International Conference on Power Electronics Systems and Applications*, pp. 1-5, 2011, doi:10.1109/PESA.2011.5982922

[22] L. Arribas, L. Cano, I. Cruz, M. Mata, and E. Llobet, "PV-wind hybrid system performance: A new approach and a case study," *Renewable Energy*, vol. 35, pp. 128-137, 2010, doi:10.1016/j.renene.2009.07.002

[23] H. Yang, L. Lu, and W. Zhou, "A novel optimization sizing model for hybrid solar-wind power generation system," *Solar Energy*, vol. 81, pp. 76-84, 2007, doi:10.1016/j.solener.2006.06.010

[24] D. K. Chy and M. Khaliluzzaman, "Experimental assessment of PV arrays connected to Buck-Boost converter using MPPT and Non-MPPT technique by implementing in real time hardware," *International Conference on Advances in Electrical Engineering (ICAEE)*, pp. 306-309, 2015, doi:10.1109/ICAEE.2015.7506856

[25] S. N. M. Rozi and S. Salimin, "Development of Hybrid Energy System for Streetlight in Ayer Hitam, Johor Using MATLAB/Simulink," *IEEE Student Conference on Research and Development (SCOReD)*, pp. 337-341, 2020, doi:10.1109/SCOReD50371.2020.9251011

[26] V. Kumari, "Modeling and analysis of hybrid renewable energy system using MPPT," *International Journal of Scientific & Engineering Research*, vol. 10, no. 5, pp. 180-186, May 2019.

[27] S. Masri, and P. W. Chan, "Design and development of a DC-DC boost converter with constant output voltage," *International Conference on Intelligent and Advanced Systems*, pp. 1-4, 2010, doi: 10.1109/ICIAS.2010.5716257.

2. MODEL DESCRIPTION

The proposed hybrid system consists of a 12kW wind turbine, and a PV array comprising of six series modules and ten parallel strings which can generate a maximum power of 12.8kW. The wind turbine connects to a DC-DC boost converter through a rectifier. This boost converter converts the input voltage from the wind turbine to 500V output. Similarly, the PV array is connected to its own DC-DC boost converter giving an output of 500V. Both these output branches are joined and fed into an inverter which is connected to the grid through an L-filter. The model was built and analyzed using MATLAB/Simulink.

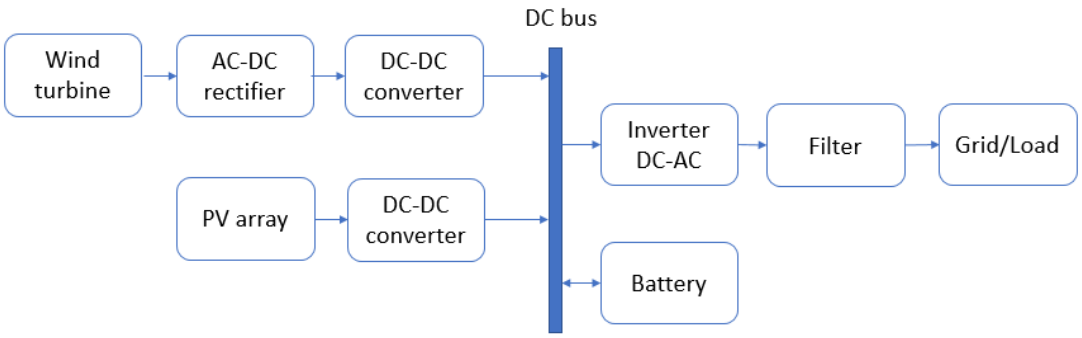

Figure 2.1. Block diagram of proposed model

Various sub-components of the proposed system are described in the following subsections.

Wind turbine

Wind speed data in climatic maps or documentations is usually presented for an altitude of 10m. The installation height of 5-12kW wind turbines is 18-36m on an average [1]. It is known that with the remoteness from the earth's surface, the wind speed increases. The wind speed at the desired height relative to the already known wind speed at a different height is calculated by using equation 2.1 [2].

$$v_2 = v_1 \left(\frac{h_2}{h_1}\right)^{\alpha} \tag{2.1}$$

where v_1, v_2 are the speeds of wind flow at the heights of $h_1$and h_2 respectively in m/s; α is the shift factor (if the value is unknown, it is assumed: α = 1/7).

The mechanical power from the wind (P_M), which is applied to blades can be determined by the following equation [3].

$$P_M = \frac{1}{2}\rho A v_2^3 C_p(\lambda, \beta) \tag{2.2}$$

where

ρ is air density which is a function of temperature, humidity and pressure and its value is taken as 1.225kg/m^3;

A is sweep area of the blades, which is determined by blade length (r_T), $A = \pi {r_T}^2$;

v_2 is wind speed in m/s at the height of blade installation;

C_p is power coefficient which is a function of ratio of rotor blade tip speed to wind speed (λ) and blade pitch angle (β) [4]. It varies from 0.2 to 0.5 [5].

The power output can be expressed in terms of torque utilizing equation 2.3 [3].

$$P_M = T_M \omega_M \tag{2.3}$$

where

T_M is mechanical torque of wind turbine, expressed in N-m

Figure 2.2a depicts the Simulink block of wind turbine which shows that it requires three input variables which are generator speed, pitch angle and wind speed. These input variables are same as the parameters required to theoretically calculate the power output using equation 2.2. In this case, the output from the WT block is per unit mechanical torque.

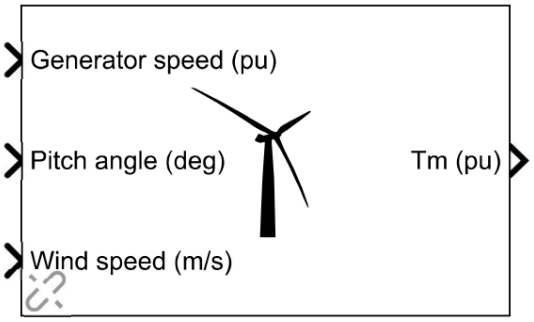

Figure 2.2a. Wind turbine block in Simulink

Figure 2.2b depicts the model under the WT block which describes the process of obtaining per unit torque from the input variables mentioned above.

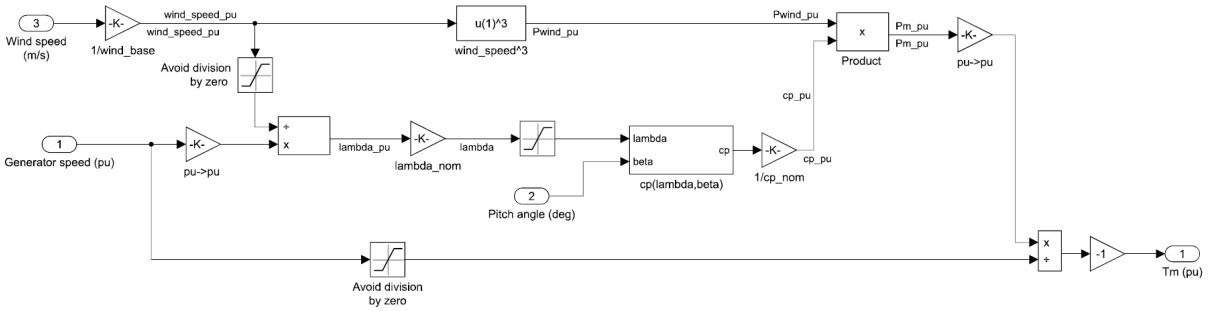

Figure 2.2b. Wind turbine model under mask of wind turbine block (2.2a)

Tip Speed Ratio:

As mentioned above, tip speed ratio is the ratio between blade tip speed and wind speed and is a vital parameter in calculating torque and output power of a wind turbine. It is calculated by the following equation:

$$\lambda = \frac{\omega_M r_T}{v} \tag{2.4}$$

where

ω_M is angular speed of wind turbine, expressed in rad/sec

Nominal value of tip speed ratio (λ_{nom}) is the value of λ when power coefficient is maximum, and as depicted in figure 2.3, it is 8.1 for the model described in figure 2.2b [6]. The maximum value of power coefficient for the model in consideration is 0.48 at pitch angle of 0°.

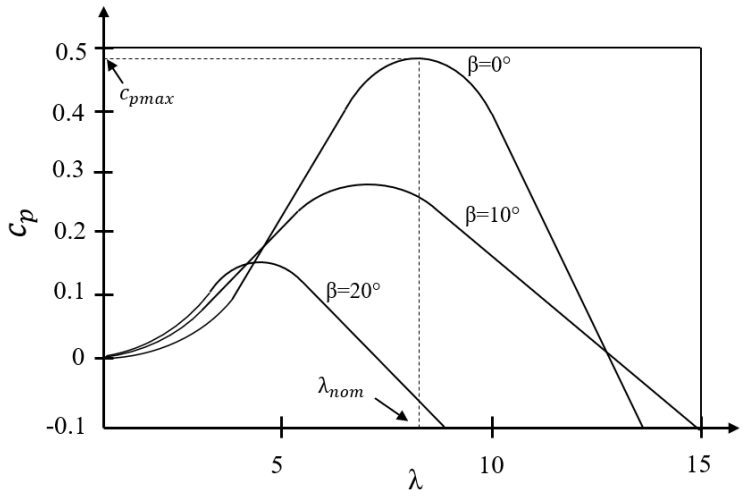

Figure 2.3. Power coefficient vs tip speed ratio graph

The input wind speed (v_2) is converted into per unit value by dividing it with base wind speed (v_{base}). In this case, rated wind speed of 12-14 m/sec is considered as the base wind speed.

$$v_{2\_pu} = \frac{v_2}{v_{base}} \tag{2.5}$$

Division of per unit generator speed by per unit wind speed provides per unit tip speed ratio (equation 2.6).

$$\lambda_{pu} = \frac{\omega_{M\_pu}}{v_{2\_pu}} \tag{2.6}$$

This per unit tip speed ratio (λ_{pu}) is then multiplied by nominal tip speed ratio (λ_{nom}) to obtain the final tip speed ratio which is further used to calculate nominal power coefficient using equation 2.7.

$$\lambda = \lambda_{pu} \cdot \lambda_{nom} \tag{2.7}$$

Generic equation used to model C_p in Simulink block for wind turbine is [2,6]:

$$C_p(\lambda, \beta) = c_1 \left(\frac{c_2}{\lambda_i} - c_3\beta - c_4 \right) e^{-\frac{c_5}{\lambda_i}} + c_6\lambda \tag{2.8}$$

where

$$\frac{1}{\lambda_i} = \frac{1}{\lambda + 0.08\beta} - \frac{0.035}{\beta^3 + 1} \tag{2.9}$$

c_1 = 0.5176; c_2 = 116; c_3 = 0.4; c_4 = 5; c_5 = 21; c_6 = 0.0068

Finally, the output power from equation 2.2 is normalized to obtain per unit power which when divided by per unit generator speed results in per unit torque.

$$T_{M\_pu} = \frac{v_{2\_pu}^3 C_{p\_pu}(\lambda, \beta)}{\omega_{M\_pu}} \tag{2.10}$$

As is evident from equations 2.2 and 2.10, the mechanical power generated by wind turbine is dependent upon the air density, wind turbine characteristics such as blade sweep area, tip speed ratio, blade pitch angle, etc., and wind speed. Involvement of multiple parameters makes it impractical and a laborious task to calculate the output power using theoretical equations [7,8]. Therefore, power curves are utilized to evaluate the performance of wind turbines.

Power curves determine the potential power output from a wind turbine at different wind speeds [9]. It is a performance indicator for the wind turbine which is provided by manufacturers to consumers. A typical wind turbine power curve is shown in figure 2.4. As depicted in figure 2.4, the power curve is divided into four regions based on the wind speed. In the first region, wind speed is below the cut-in speed, i.e.it is under the minimum speed required by the wind turbine to produce any power. The second region lies between cut-in speed and rated speed. The rated wind speed is the speed at which the installation starts producing rated power [3]. The third region lies between the rated and cut-out speeds where the cut-out speed is the maximum speed at which the wind turbine can operate without any damage. The wind turbine produces constant rated voltage until it reaches the cut-out speed [9]. Finally, in the fourth region, the wind turbine shuts down because the wind speed increased beyond the cut-out speeds and therefore, no power is generated.

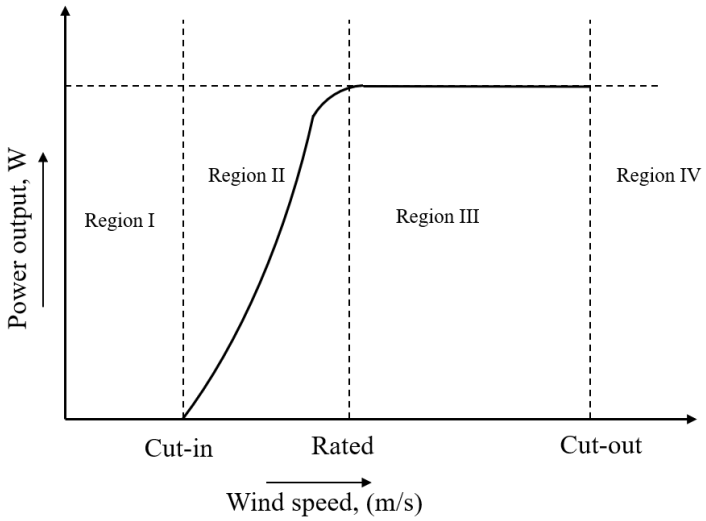

Figure 2.4. Wind turbine power curve

In order to choose the appropriate wind turbine, it is required to obtain information on monthly or daily average wind speeds in the expected location (v, m/s); select the desired type of wind turbine and find its technical characteristics such as the power curve ($P_M = f(v)$, W) ; choose the desired height of the blades installation (h, m); and set the monthly amount of energy consumption ($P_{con.}$, kWh). Once the aforementioned parameters are determined, the following steps must be taken into consideration to choose wind turbine for a particular area:

1. Recalculate wind speed (v_2, m/s) at the height of blades installation (h, m) by using equation 2.1.

2. Based on the recalculated wind speed v_h, and wind turbine power curve, the potential amount of energy generated by the wind turbine must be calculated by equation 2.11

$$P_{wt.out} = \left(P_{M\_v_h} \cdot 24 \cdot n_d\right)/1000 \quad (2.11)$$

where $P_{wt.out}$ is the amount of energy generated by the wind turbine per month (kWh); $P_{M\_v_h}$ is the energy obtained from the power curve for the wind speed v_h; and n_d is number days in the month.

3. Finally, generated energy ($P_{wt.out}$) and required energy ($P_{con.}$) must be compared. In case $P_{wt.out} > P_{con.}$ chosen WT is able to cover the energy requirement. Otherwise, the same calculations must be conducted with higher wind turbine height or higher rated power.

The wind turbine selection process is summarized in the figure 2.5.

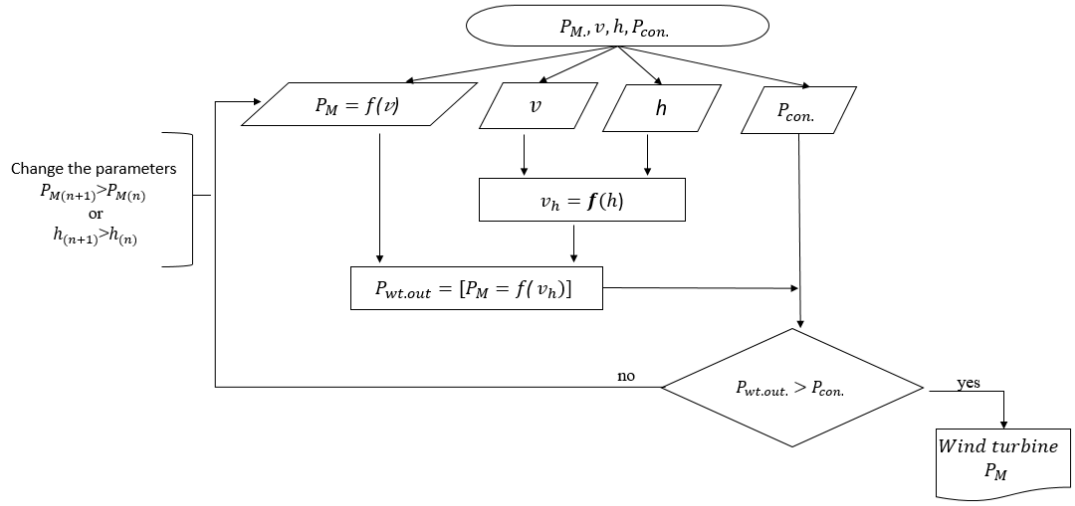

Figure 2.5. Flowchart for wind turbine selection

Figure 2.6 shows the power characteristics of selected wind turbine at pitch angle of 0°. The pitch angle always remains 0° because maximum power point tracking was not used for the wind energy system.

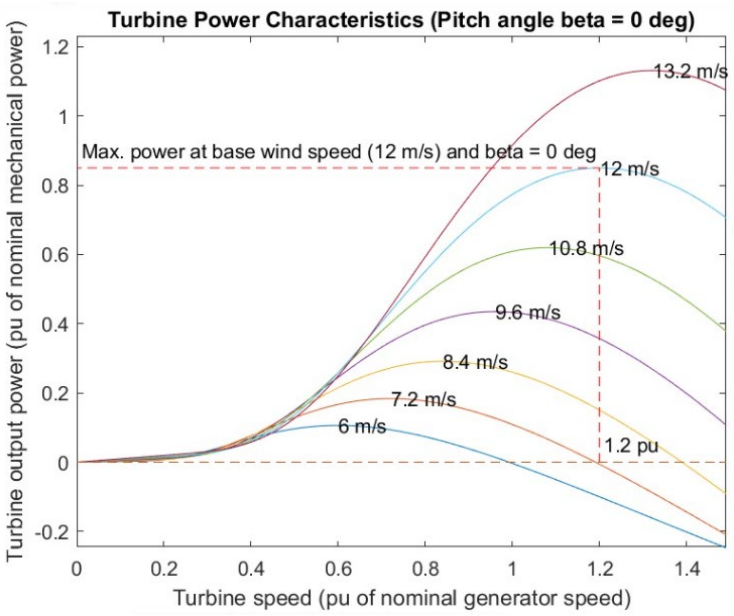

Figure 2.6. Power characteristics of wind turbine at 0° pitch angle

Permanent Magnet Synchronous Generator (PMSG)

PMSGs are often employed in small and medium-scale wind turbines due to higher efficiency, lower maintenance, reliable power generation, and lower downtime as compared to induction generators [10]. Direct-drive PMSGs do not require installing a gearbox which considerably reduces both the maintenance time and expenses since gearbox malfunctioning is responsible for more than 19% of downtime in wind turbine generators [10,11]. Furthermore, absence of rotor current and consequently lack of copper losses in the rotor circuit leads to higher efficiency of PMSGs [11]. Therefore, PMSG was used in the hybrid model developed in this study.

Permanent magnet synchronous machine block in Simulink was used to simulate the selected generator. This block can be utilized in either generator or motor mode. In case of this research, the generator mode was implemented and therefore, it is referred to as permanent magnet synchronous generator throughout the thesis.

Stator windings are wye connected to an internal neutral point. Back electromotive force (EMF) waveform used is sinusoidal which leads to sinusoidal flux being established by the permanent magnets. Therefore, electromotive forces are sinusoidal too. The generator is modeled in dq-form and therefore has no AC states modeled in the system [11]. The equations for modeling d-axis and q-axis current are given by [12]:

$$\frac{di_d}{dt} = \frac{1}{L_d}[v_d + p\omega_g L_q i_q - R_d i_d] \quad (2.12a)$$

$$\frac{di_q}{dt} = \frac{1}{L_q}[v_q - p\omega_g(L_d i_d + M i_f) - R_q i_q] \quad (2.12b)$$

The electromagnetic torque (T_e) can be calculated by using equation 2.13 [13]:

$$T_e = 1.5p[\Phi_m i_q + (L_d - L_q) i_d i_q] \quad (2.13)$$

where

i_d and i_q are d-axis and q-axis stator currents respectively;

v_d and v_q are d-axis and q-axis stator voltages respectively;

L_d and L_q are d-axis and q-axis stator inductances respectively;

R_d and R_q are d-axis and q-axis stator resistances respectively;

p is the number of PMSG pole pairs;

ω_g is electric angular frequency of generator;

M is mutual inductance;

i_f is equivalent rotor current;

Φ_m is flux linkage generated by permanent magnet.

Due to low speed operation of PMSG in wind turbines, salient pole rotor is employed. Furthermore, the lower manufacturing cost of salient pole machines as compared to non-salient pole machines is an additional benefit [14]. For salient pole rotors, d-axis and q-axis stator induction is given by [14]:

$$L_d = \frac{L_{d\_max}}{2} \quad (2.14a)$$

$$L_q = \frac{L_{q\_min}}{2} \quad (2.14b)$$

where

L_{d_max} and L_{q_min} are maximum d-axis inductance and minimum q-axis inductance respectively.

Photovoltaic System

Radiation intensity and temperature affect the current–voltage (I–V) characteristics of a PV panel. The short-circuit current (I_{sc}) generated by the PV panel is affected by radiation intensity and the rate of change of short-circuit current is higher

than that of open-circuit voltage (V_{oc}). Similarly, the short-circuit current of a solar panel is directly proportion to radiation at a given temperature. If radiation is kept constant, the short-circuit current increases and the open-circuit voltage reduces as the temperature rises. Therefore, it is vital to analyze the effect of radiation intensity and temperature in order to design an efficient PV energy system.

Based on the initial requirements of the system to provide 12kW power, 60 modules were chosen with each module generating 213.5W. In order to obtain the required output power, the modules were connected in series and parallel combinations to produce solar panels at desired voltage and current values. The designed PV system consists of ten strings in parallel with each having six modules in series. The general output current equation is:

$$I = I_L - I_0[\exp\left(\frac{qV}{nkT}\right) - 1] \tag{2.15}$$

where I_0 is the current when there is no light on the cell, I_L is the current generated by light, q is electron charge, T is absolute temperature, and k is the Boltzmann's constant [15]. The I-V and P-V characteristics of the chosen PV panels are presented in figures 2.7a and 2.7b.

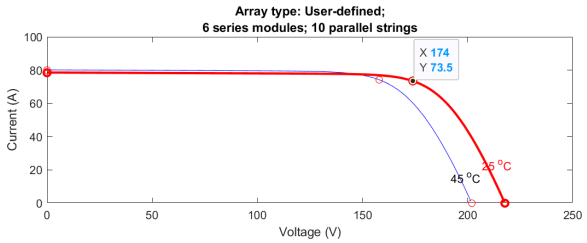

Figure 2.7a. I-V curve

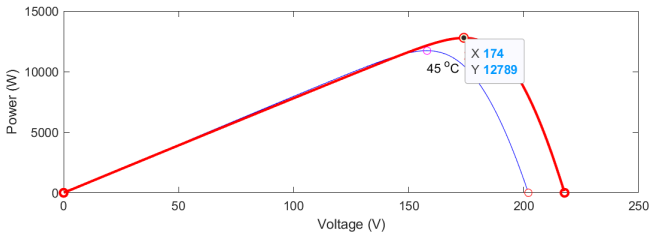

Figure 2.7b. P-V curve

From the I-V curve, the maximum current of the cells at zero voltage (short circuit current) was determined to be $I_{sc} = 78.4A$ and maximum voltage of the cells at zero current (open circuit voltage) was $V_{oc} = 217.8V$

Power out of the cells was calculated by multiplying voltage and current at a specific point on the curve. Furthermore, the P-V curve showed that the maximum power of the cell, characterized by maximum power point, was $P_{mpp} = I_{mpp}.V_{mpp} =$ 12.789kW, where $I_{mpp} = 73.5$ A and $V_{mpp} = 174\,V$.

Figure 2.8a depicts the Simulink block of PV array which shows that it requires two input variables which are irradiance (I_r) and temperature (T). The output terminal (m) can be used for measuring diode voltage, PV voltage and PV current. Figure 2.8b illustrates the model under the PV array block which consists of four parameters – a light-generated current source (I_L), diode, series resistance (R_s), and shunt resistance (R_{sh}). These parameters represent the I-V characteristics of the module which depend upon the two input variables.

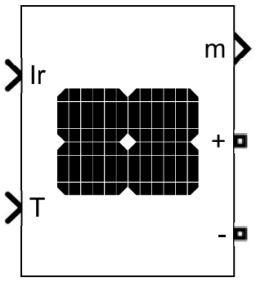

Figure 2.8a. PV array Simulink block

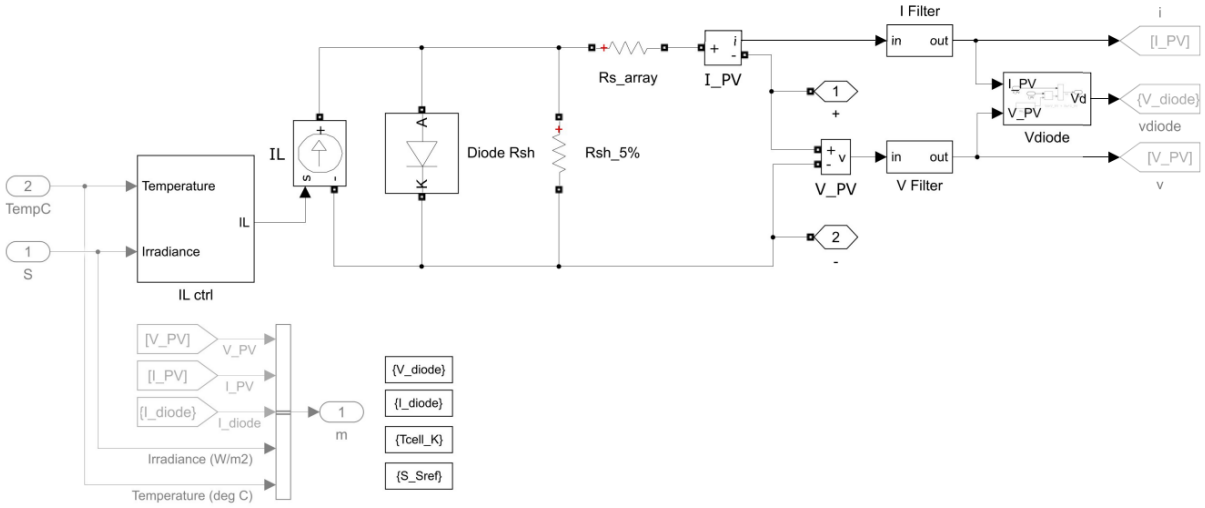

Figure 2.8b. Model under PV array Simulink block mask

DC-DC Boost converter

Numerous devices, including PV and wind energy-based power systems, require the utilization of DC to DC converters. Buck converters, boost converters and buck-boost converters are three major types of non-isolated DC-DC converters [16]. Buck converters step-down the input voltage in order to generate a lower output voltage [16]. Conversely, boost converters step-up the input voltage leading to a higher output voltage [16]. Buck-boost converters are capable of both stepping-up and stepping-down voltages, which means that the magnitude of output voltage is either greater than or less than that of input voltage [16]. The boost converter is one of the most important components used in the design of this hybrid power system.

As previously mentioned, one DC-DC boost converter each was connected to the PV and wind energy sub-topologies of the system. The output voltage from both the boost converters is required to be 500V for the systems to operate as desired. Figure 2.9a depicts the configuration of an ideal DC-DC boost converter. An ideal converter does not take losses into consideration and additional resistances are added to simulate losses, as shown in figure 2.9b. Voltage conversion ratio (M) of any dc-dc converter is the ratio of output to input voltage and is given by equation 2.16 [17].

$$M = \frac{V}{V_g} = \frac{1}{1 - D} \tag{2.16}$$

where

V is the output voltage;

V_g is the input voltage;

D is the duty cycle

It can be noted from equation 2.16, that output voltage is equal to input voltage when duty cycle is zero. The output voltage tends to infinity as the duty cycle approaches one, meaning that theoretically an ideal boost converter can produce any value of output voltage greater than input voltage [17]. But practically, the maximum output voltage of a boost converter is constrained by the loss elements such as semiconductor on-resistances, inductor winding resistance, etc. (figure 2.9b).

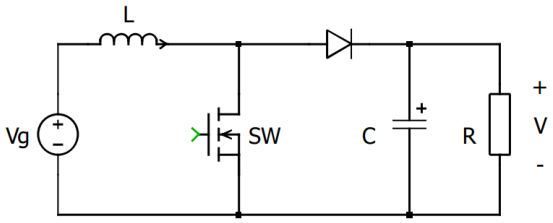

Figure 2.9a. Ideal DC-DC boost converter

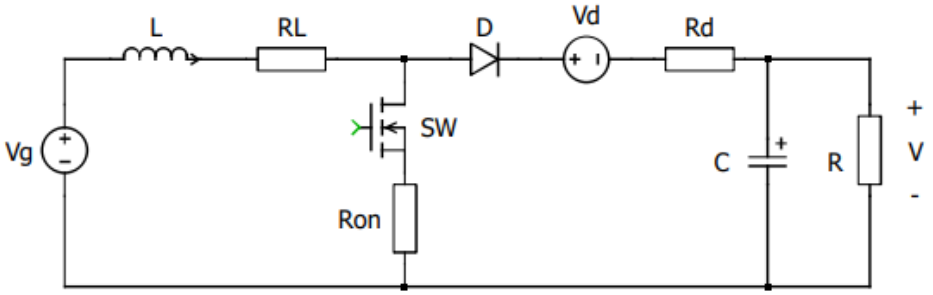

Figure 2.9b. DC-DC boost converter with additional resistance (losses)

There are two switching modes with the switch (SW) in ON position (figure 2.10a) and in OFF position (figures 2.10b).

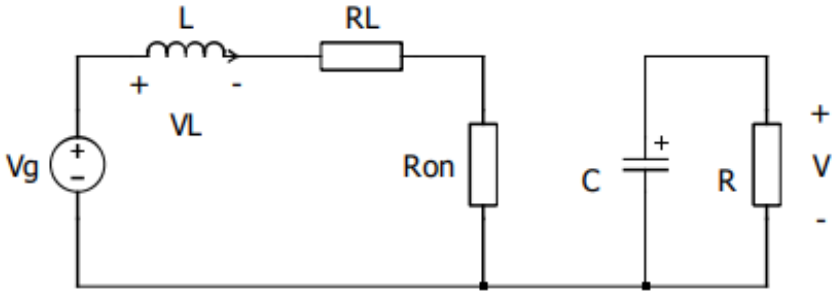

Figure 2.10a. Boost converter subinterval 1: Switch ON

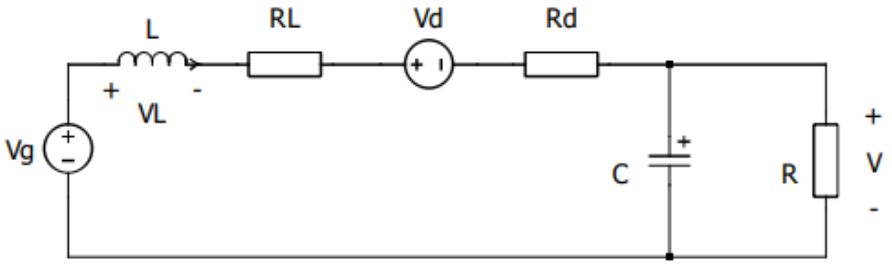

Figure 2.10b. Boost converter subinterval 2: Switch OFF

Inductor voltage and capacitor current equations for subinterval 1 and subinterval 2 are presented in equations 2.17 and 2.18.

Subinterval 1:

$$V_L = V_g - IR_L - IR_{on} \tag{2.17a}$$

$$i_C = -\frac{V}{R} \tag{2.17b}$$

Subinterval 2:

$$V_L = V_g - IR_L - V_D - IR_D - V \tag{2.18a}$$

$$i_C = I_L - \frac{V}{R} \tag{2.18b}$$

Volt-second balance:

$$V_g - IR_L - IDR_{on} - D'V_D - ID'R_D - D'V = 0 \tag{2.19}$$

The ratio of output to input voltage is given by the volt-second balance equation (equation 2.20).

$$\frac{V}{V_g} = \frac{1}{D'}\left[1 - \frac{D'V_D}{V_g}\right]\frac{1}{1 + \frac{R_L + DR_{on} + D'R_D}{D'^2R}} \tag{2.20}$$

where V_D is the forward voltage drop on the diode, R is the resistance due to load, R_{on} is switch on-resistance, R_L is the parasitic resistance of the inductor and R_D is the forward on-resistance of the diode. Ideal boost converter was used to facilitate further calculations. Inductor current, I_L is given by capacitor charge balance equation (Equation 2.21), which was utilized to determine the boundary conditions and calculate minimum inductance.

$$I_L = \frac{VD'}{R} \tag{2.21}$$

Boost converter can operate in continuous conduction mode (CCM) and discontinuous conduction mode (DCM). The boundary conditions between the two modes can be determined by value of inductor current (I_L) and inductor current ripples (Δi_L). If $I > \Delta i_L$, then the converter is working in CCM and if $I < \Delta i_L$, then it is

operating in DCM. Based on these boundary conditions, the equation for inductance was determined and solved to find the inductance value (Equation 2.22).

$$L = \frac{DD'^2V^2}{P_{out}} \tag{2.22}$$

where P_{out} is the output power from the boost converter. For CCM, inductance was chosen 50 times more than the boundary condition and was calculated to be 0.0082H in case of boost converter for PV sub-system. Similarly, for the WECS boost converter, the inductance was found out to be 1.875×10^{-5} H.

Capacitance, C was calculated using equation 2.23 and its value for both boost converters was 1μF.

$$C \geq \frac{DP_{out}}{2V\Delta V f_{sw\_boost}} \tag{2.23}$$

where f_{sw_boost} is switching frequency of the boost converter and ΔV is voltage ripple

Proportional-Integral-Derivative (PID) controller

It is vital to reduce the steady state error and overshoot in output voltage of boost converters. One method to achieve zero steady state error and minimum overshoot is to employ a PID compensator. A PID compensator consists of a combination of three control systems – proportional, integral and derivative systems. Proportional control systems feed the error forward to the plant, integral control systems feed the integral of the error to plant, and derivative control systems feed the derivative of the error to plant [18]. The steady state error can be minimized or reduced to zero by implementing an ideal integral compensator. An ideal integral compensator also requires the error to be fed forward and therefore, is also referred to as proportional-integral (PI) compensator. Transient response which includes percent overshoot and settling time can be improved by implementing an ideal derivative compensator, which is commonly referred to as proportional-derivative (PD) compensator because using it requires feeding the error as well as the derivative of error forward to the plant. In order to improve both steady-state error and transient response, a PD controller followed by a PI controller must be designed [18]. The result of this combination of PD and PI controllers is called the PID compensator.

MPPT Algorithms

The Maximum Power Point Tracking (MPPT) algorithms are widely utilized to effectively track, extract and maintain maximum available power from a PV system [19]. The non-linear I-V and P-V characteristics of a solar panel depends on multiple environmental factors such as irradiance and ambient temperature [20]. In order to obtain maximum power from PV modules, they must be operated at a maximum power point irrespective of weather conditions. This maximum power point is, therefore, not a fixed point on the P-V curve but transposes on the curve depending upon the weather conditions [21]. The MPPT techniques are employed to generate pulse width modulated (PWM) signals in order to vary the duty ratio of DC-DC boost converter [22,23].

Various types of MPPT algorithms have been developed and implemented in literature to operate the PV module at its maximum power point. Some of the commonly used techniques are briefly explained below:

Incremental conductance (INC) method: INC is a widely acceptable MPPT technique because of its highly accurate tracking at steady state. This algorithm is based on the fact that the slope of the P-V curve is zero at the maximum power point i.e. at this point there is no change in power with respect to output voltage [24]. Furthermore, the slope is positive for output voltage values below the maximum power point and negative for output voltage values above it [24]. The algorithm tracks the instantaneous (I/V) and incremental conductance (dI/dV) of the PV array. It is established that at maximum power point: $dI/dV = -I/V$; at output voltage values below the maximum power point $dI/dV > -I/V$ and at output voltage above it $dI/dV < -I/V$ [25]. Another popular modified version of this method utilizes the PV panel current instead of voltage because the variation in voltage reduces significantly towards the right side of the maximum power point which could lead to negligible change in voltage in two consecutive sampling instances [26].

Constant Voltage (CV) algorithm: CV method for MPPT is one of the easiest to implement. In this technique, open-circuit voltage (V_{oc}) is calculated by turning off the PV panel current to zero for a very short duration. V_{oc} is then multiplied by a proportionality constant (approximately 0.8) to calculate the required maximum power point voltage (V_{mpp}). Finally, the output voltage of PV array (V_{pv}) is calculated and controlled by pulse width modulation such that $V_{pv} = V_{mpp}$ [27].

Fuzzy Logic Controller (FLC) technique: FLC is one of the various artificial intelligence (AI) based methods for maximum power point tracking. Some other AI-based methods include artificial neural networks, particle swarm intelligence, etc. [28]. The key benefit of using FLC is its low-reliance on the accuracy of mathematical model and on input precision [24]. The logic of conventional MPPT algorithms consists of variables in only two states – true and false. In fuzzy logic, variables have a range between the true and false binary and such variables are called fuzzy variables. So FLCs for MPPT generate fuzzy input variables by interpreting PV voltage and current signals. These fuzzy variables are used to calculate duty cycles which is further controlled to obtain the maximum power point [23].

Perturb & Observe (P&O) algorithm: P&O is the most well-established and widely used method to track the maximum power point of a PV system [23]. This method is based on perturbing the output voltage of the PV system in order to produce a perturbed power which is further analyzed to calculate maximum power point. The flowchart shown in figure 2.11 depicts the P&O MPPT algorithm in detail and the method is briefly explained below:

i) The output voltage and current from the PV array are first measured and are multiplied to obtain the output power.

ii) Change in power (ΔP) is then measured. If $\Delta P=0$, then the PV array is operating at maximum power point.

iii) If $\Delta P<0$, then the algorithm checks the change in voltage. If ΔV come out to be less than 0, then it means that the reducing voltage is leading to reduction in power and therefore, in order to increase the power, the voltage must be increased by the given step-size value represented as K [19].

iv) Similarly, if $\Delta P<0$ and the algorithm measures that $\Delta V>0$, then it means that the increasing voltage is causing the reduction in power. Hence, the voltage must be increased to increase power.

v) On the other hand, if the change in power is positive, i.e. $\Delta P>0$, and algorithm verifies that $\Delta V<0$, this means than reduction in voltage is increasing the power. It will then continue to reduce the voltage so that the power continues to increase.

vi) In the final scenario, if $\Delta P>0$ and $\Delta V>0$, then the algorithm continues to increase the voltage for the power to increase.

vii) The algorithm repeats the process continuously to ensure that the operating point of the PV array achieves and continues to stay on the maximum power point.

To summarize, if perturbed power perturbation is less than the initial value, then the direction of perturbation of operating voltage is reversed to find the maximum power and if it is more than the initial value then voltage perturbation is continued in the same direction until we reach the maximum power point [23]. Figure 2.12 depicts the P-V characteristics curve of P&O algorithm, as explained above.

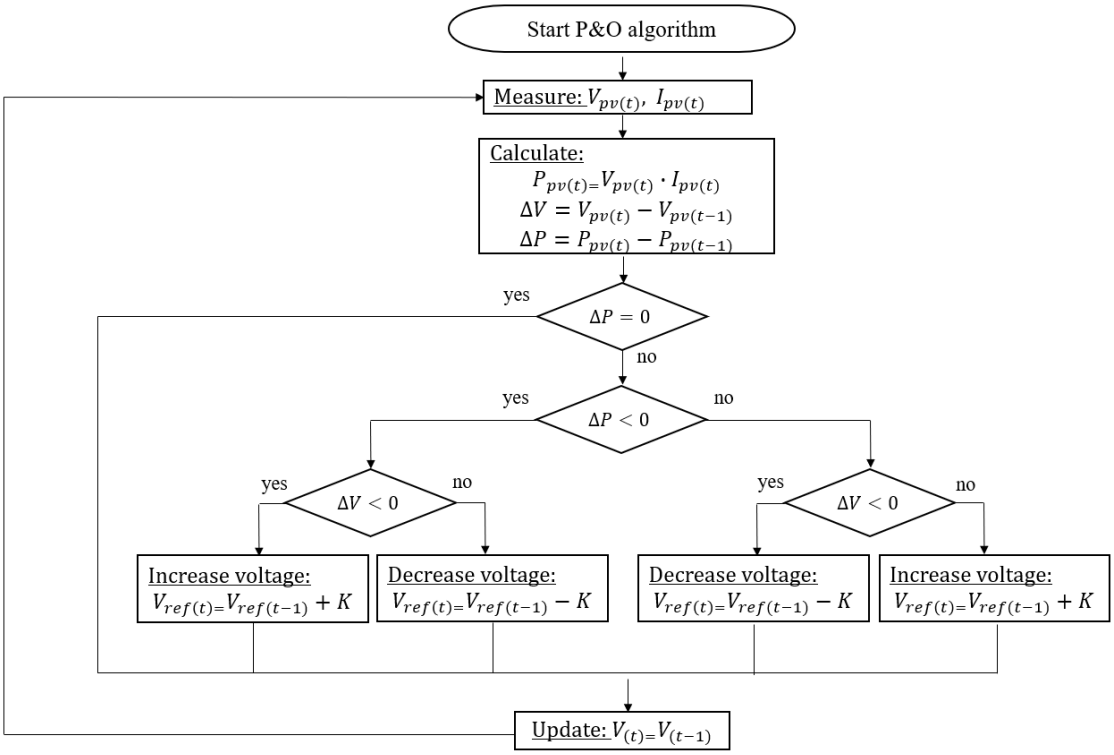

Figure 2.11. P&O Algorithm

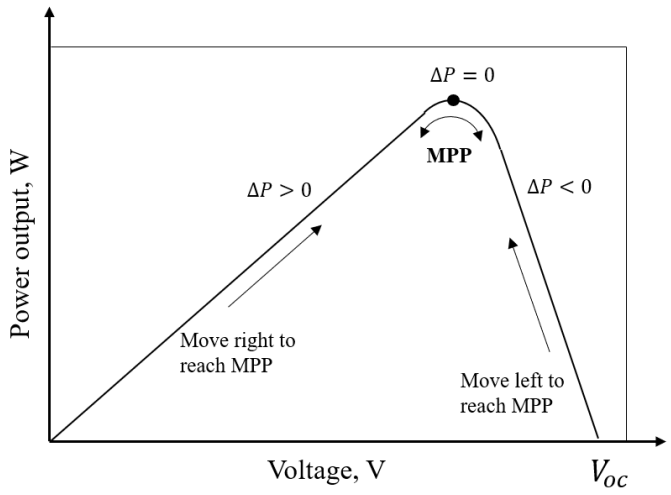

Figure 2.12. P-V characteristics of P&O algorithm

P&O algorithm was adapted for this model due to its cost-effectiveness, uncomplicated structure, involvement of fewer parameters, and ease of implementation [29]. P&O algorithm code, based on the figure 2.11, was written in Matlab to obtain the maximum power point. The algorithm was embedded into the Simulink model of P&O MPPT as shown in figure 2.13. PV voltage and current are fed into the MPPT algorithm to obtain the reference voltage V_{ref} which is the voltage at maximum power point. Therefore, V_{ref} is equal to V_{mpp} the value of which is 174V for the designed model. Unit delay block was implemented to hold and delay the input signal, i.e. PV voltage and PV current, by sampling time which is 10^{-5} seconds. Therefore, this block is used to discretize the voltage and current signals in sampling time. The initial condition for both unit delay blocks was set as zero, which means that the simulation output was set as zero for the first sampling time when it is otherwise undefined.

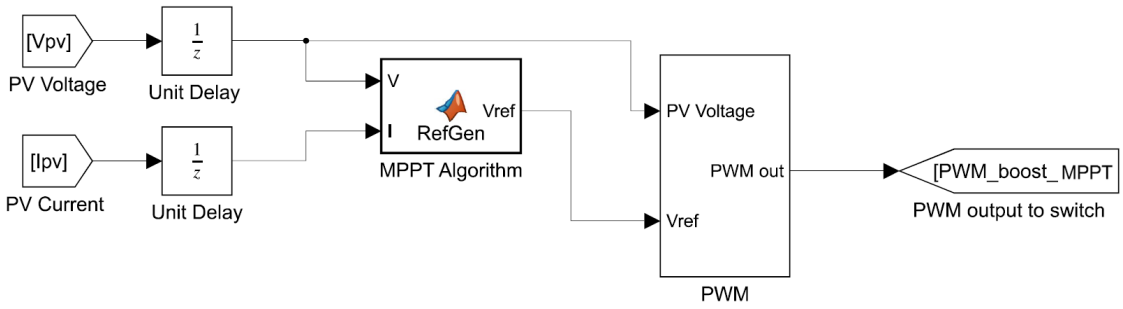

Figure 2.13. Simulink Model of P&O MPPT

PWM signal generator was implemented to generate pulses that were used as an input to switching-transistor of boost converter. PWM generator generates pulses for

carrier-based pulse width modulated converters by using two signals - reference signal and carrier signal. For the designed system, the input dc signal was used as reference and a repeating sequence block was used to obtain the triangular carrier signal. As shown in figure 2.14, a PI compensator is commonly implemented within the PWM control with the primary objective of reducing the steady-state error [30]. In addition to the low steady-state error, the PI compensators are widely used because they are easy to configure, easy to implement and are relatively inexpensive [30].

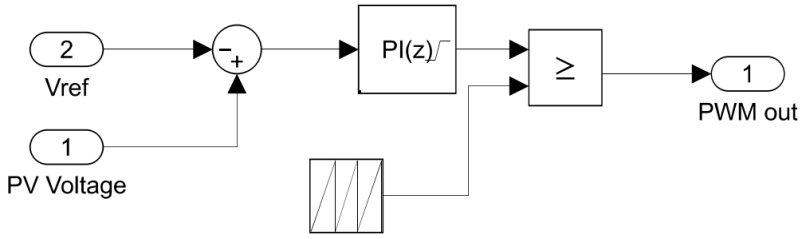

Figure 2.14. Simulink Model of PWM signal generator

The complete PV model with boost converter and MPPT but without PI controller is depicted in figure 2.15. The output power from PV array and after implementing the boost converter is shown in figures 2.16a and 2.16b. It can be inferred from these graphs that it is possible to obtain close to the desired 12.8 kW power at the rated irradiance of 1000 W/m^2 without implementing the PI controller and therefore, due to MPPT we are able to obtain maximum power out of the system.

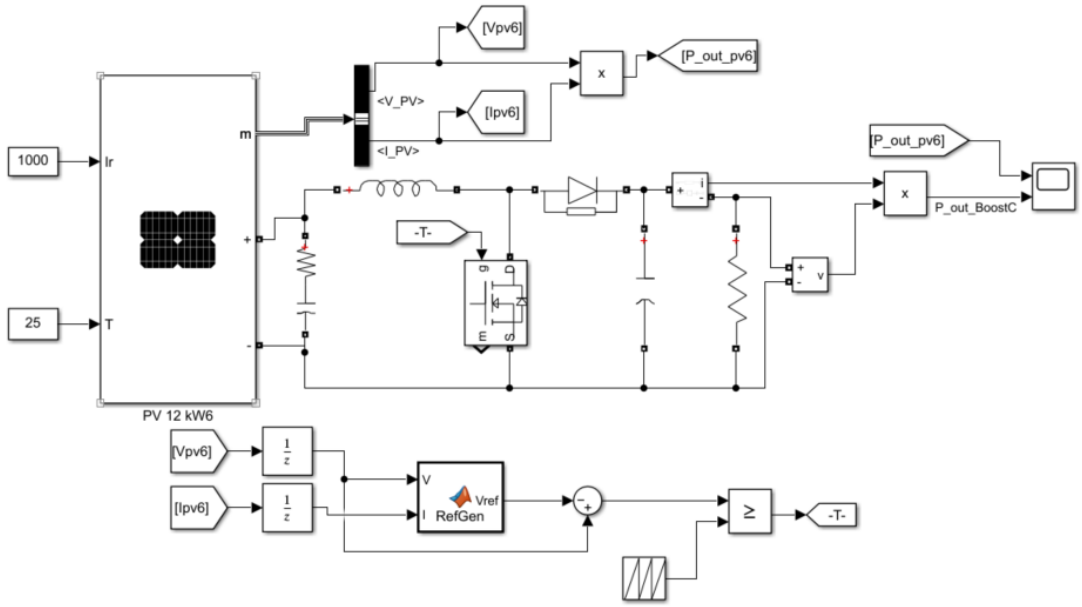

Figure 2.15. Simulink model of boost converter with P&O MPPT

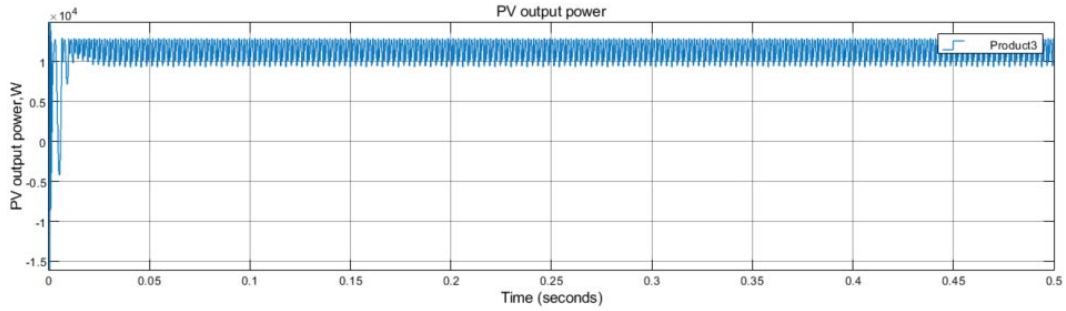

Figure 2.16a. Power output from PV array with P&O MPPT without PI controller

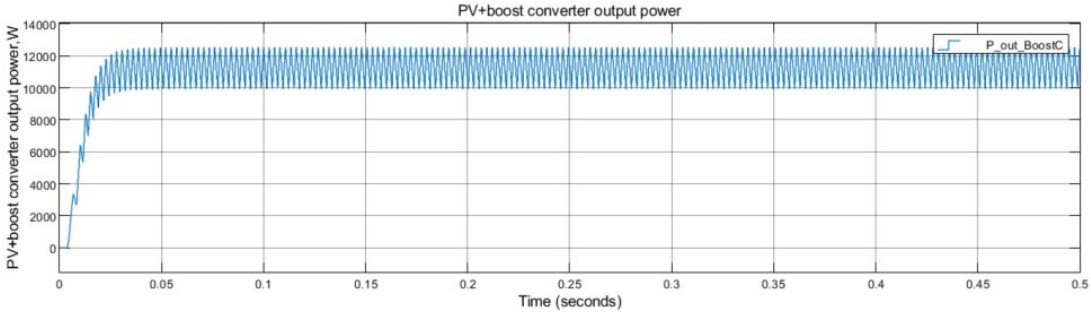

Figure 2.16b. Power output from boost converter with P&O MPPT without PI controller

Although it was possible to obtain an output power close to the required value of 12.8 kW without implementing PI controller, large ripple was observed, and the steady-state error could still be reduced in order to get a more stable output. Figure 2.17 depicts the final PV model with boost converter, MPPT and PI controller which was implemented in the proposed hybrid system. As shown in figure 2.18b, the output power from the boost converter, which is further fed to dc bus, was 12.8 kW with low ripples and close to zero steady-state error. The resulting power output at various irradiance levels is depicted in figures 2.19a and 2.19b with the figures showing output power from the PV array and from boost converter with MPPT and PI controller installed respectively.

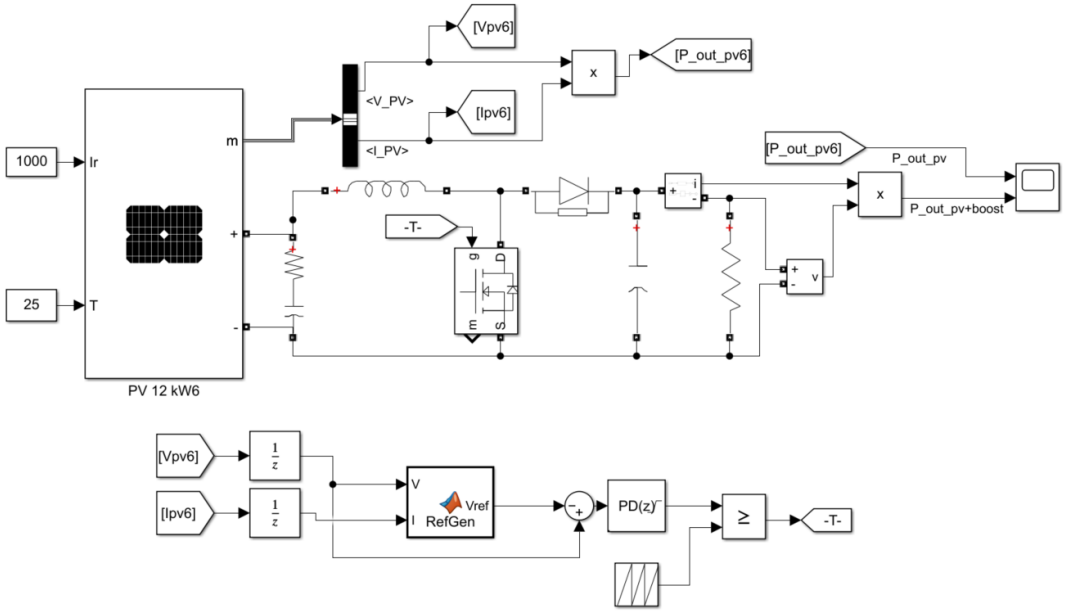

Figure 2.17. Simulink model of boost converter with P&O MPPT+PI controller

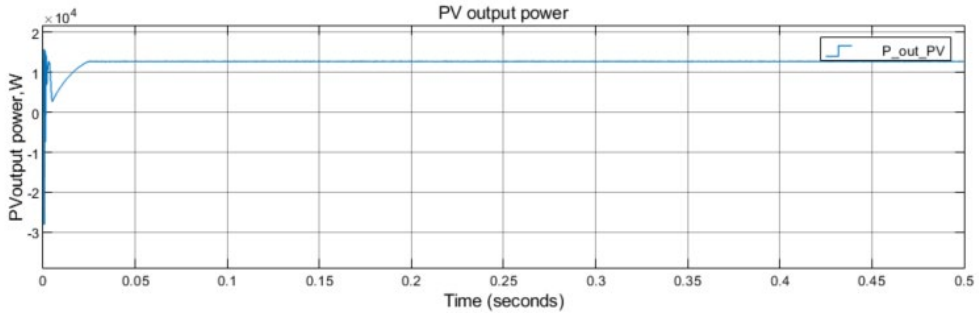

Figure 2.18a. Power output from PV array with P&O MPPT + PI controller

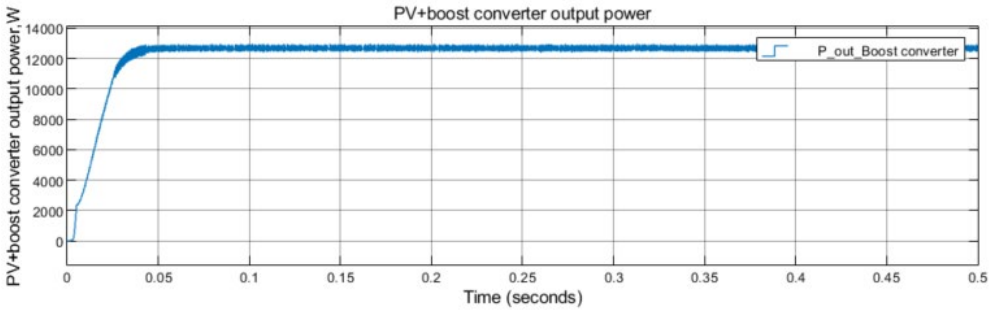

Figure 2.18b. Power output PV+ boost converter +MPPT+PI under constant irradiance 1000W/m^2

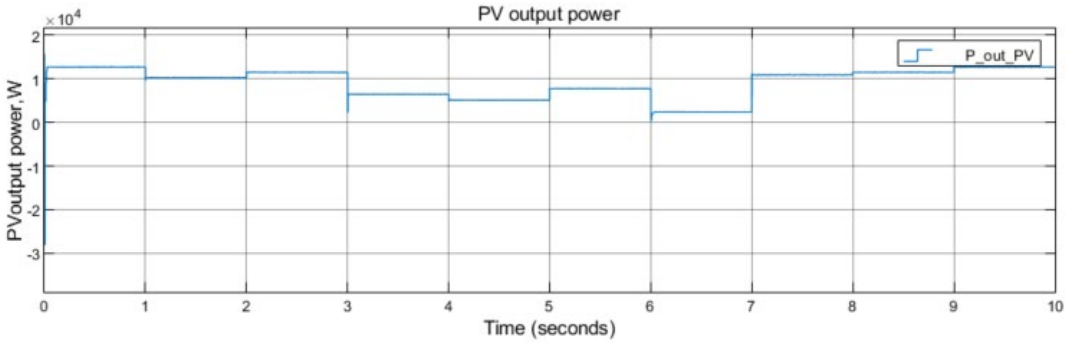

Figure 2.19a. Power output from PV array under step change irradiance

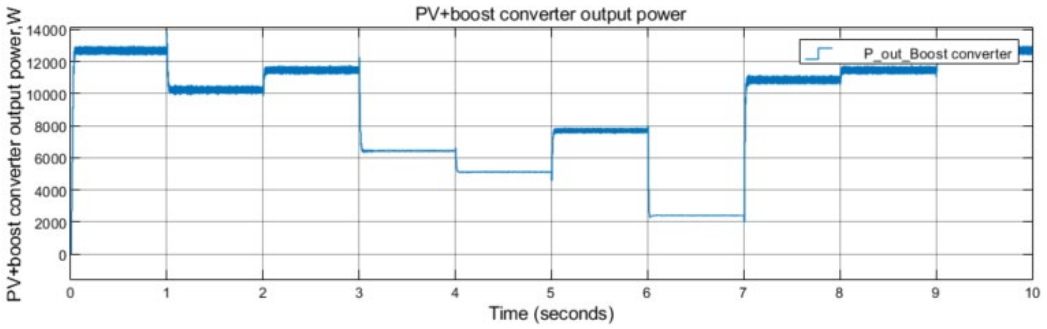

Figure 2.19b. Power output PV + boost converter + MPPT + PI under step change irradiance

Filter

Various types of harmonic filters are utilized in WECS and PV energy conversion systems to solve the issue of switching harmonics generated by power converters [31]. Three main filter alternatives are L, LCL, and LC filters. L-filters (figure 2.20a) are generally employed in generator side converters and therefore, help to reduce harmonic distortion in generator voltage and current [31]. LCL-filters (figure 2.20c) are often used in the grid-side converters and are the most efficient out of the three filter types. LC-filters (figure 2.20b), although not as effective as LCL-filters, are commonly employed in wind and PV systems [31]. Furthermore, L-filters are also widely used for inverters and were chosen for the designed hybrid system [32].

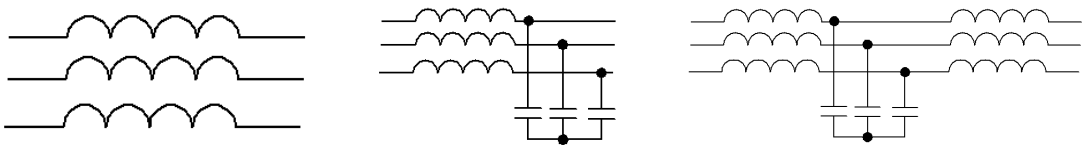

Figure 2.20 (a) L-filter (b) LC-filter (c) LCL-filter

The inductor selection depends on the ripple current, switching losses, conduction losses, inductor losses and core losses [33]. The larger the inductor, the larger would be the inductor and core losses. The ripple current is usually chosen to be 10-25% of rated current [33] and therefore, for this analysis a ripple current of 10% of rated current was considered. The filter inductance (L_f) is calculated as:

$$L_f = \frac{1}{8}.\frac{V_{dc}}{0.1 i_{rated}.f_s} \tag{2.24}$$

where

V_{dc} is dc-dc boost converter output voltage (V);

i_{rated} is rated current (A);

f_s is the switching frequency (Hz).

In case an LC-filter is required to be implemented, the capacitor value must also be calculated. The capacitor selection is balance between the reactive power in capacitor and filter inductance [33]. Considering reactive power to be 10% of rated power, the filter capacitance (C_f) is given by:

$$C_f = \frac{0.1 P_{rated}}{3.2\pi f.V_{rated}^2} \tag{2.25}$$

Inverter

The electricity generated by the PV and wind systems could be directed to the grid through an inverter. The direct current from the PV and wind energy subsystems was converted to alternating current by using a 3-phase inverter which was then connected to the grid. There are various schemes to control a grid-connected inverter and voltage-oriented control (VOC) was utilized for this analysis [34]. Figure 2.21 shows the control structure of a three-phase grid-tied inverter. VOC is based on transformation between the abc stationary reference frame and dq synchronous frame [34]. VOC is achieved by first calculating grid voltage and its angle θ_g. Theoretically, θ_g can be calculated using:

$$\theta_g = \frac{V_{ga}}{\frac{1}{\sqrt{3}}(V_{ga} + 2V_{gb})} \tag{2.26}$$

where

V_{ga} and V_{gb} are phase-a and phase-b grid voltages

But practically, θ_g is calculated by using phase-lock loops because of distortion in grid voltage due to presence of harmonics. θ_g is used for the transformation of variables from abc to dq frames through the abc/dq transformation or from dq to abc frames through the dq/abc transformation [34]. As depicted in figure 2.27, the three-phase line currents in the abc-frame (i_{ga}, i_{gb}, and i_{gc}) are transformed to two-phase currents (i_{gd} and i_{gq}) in the dq-frame.

The inverter power flow is in two directions which means that when the power is transferred to grid, it operates as an inverter whereas when power is transferred from grid to dc-circuit, then it works in rectifying mode [34]. Since the voltage-oriented control system can switch between both inverting and rectifying modes automatically, therefore no design update is required to accommodate bidirectional power flow. Finally, the inverter output current was filtered by passing through an L-filter and produced the grid-side three-phase current (i_{ga}, i_{gb}, i_{gc}).

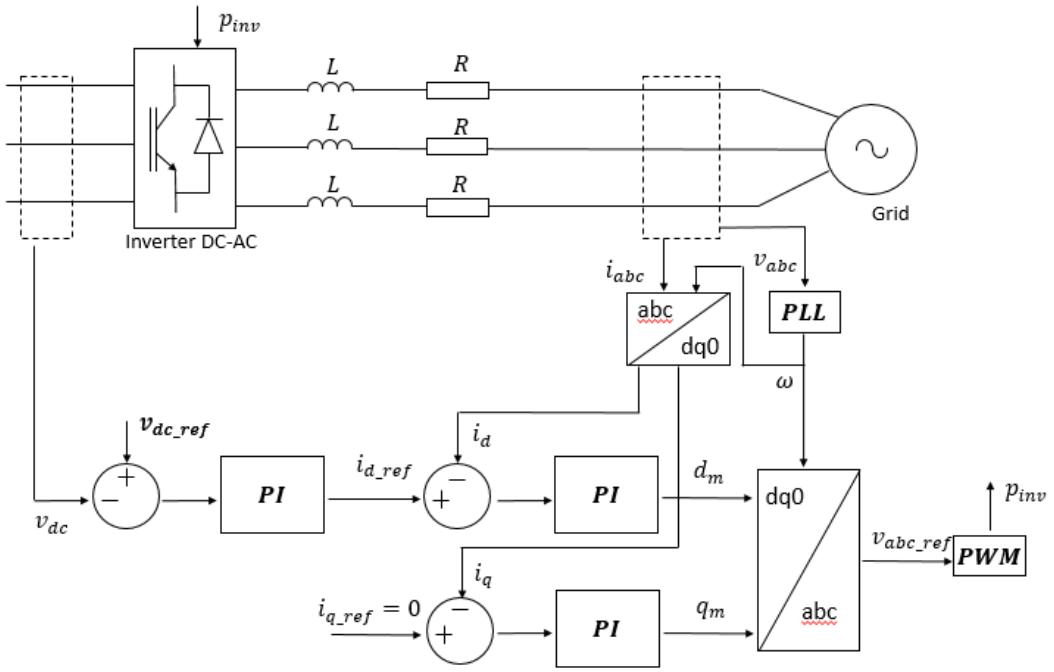

Figure 2.21. Grid-tied inverter control schematic

Inverter Requirements

Hong et. al. [35] specified four prerequisites for the inverter to be able to attain the control objectives:

i) It is vital for the inverters implemented in standalone PV, standalone wind or hybrid energy generation systems to be robust due to the random nature of input solar irradiance, wind speeds and other environmental conditions.

ii) The inverter phase and frequency must match the grid-side voltage.

iii) The inverter power active power (P) and reactive power (Q) must follow the expressions:

$$P = \frac{3}{2}(I_{gd}V_{gd} + I_{gq}V_{gq}) \tag{2.27a}$$

$$Q = \frac{3}{2}(I_{gq}V_{gd} + I_{gd}V_{gq}) \tag{2.27b}$$

where

V_{gd} and V_{gq} represent grid voltage in dq-axis;

I_{gd} and I_{gq} represent inverter output current in dq-axis.

iv) It is crucial to keep the harmonic components of output current from the inverter below a specific rate. Upper-order harmonics can be eliminated by the LC filter whereas the lower order harmonics can be reduced but not eliminated with the filter.

Another important parameter to take into consideration is the inverter conversion efficiency which is the ratio of output power (P_{out}) to input power (P_{in}), i.e.

$$\eta_{inv} = \frac{P_{out}}{P_{in}} \tag{2.28}$$

Average model of voltage source inverter (VSI)

Average model of voltage source inverter was derived from simplifying the switching model of VSI (figure 2.22). The steps followed to derive the averaged model are depicted below:

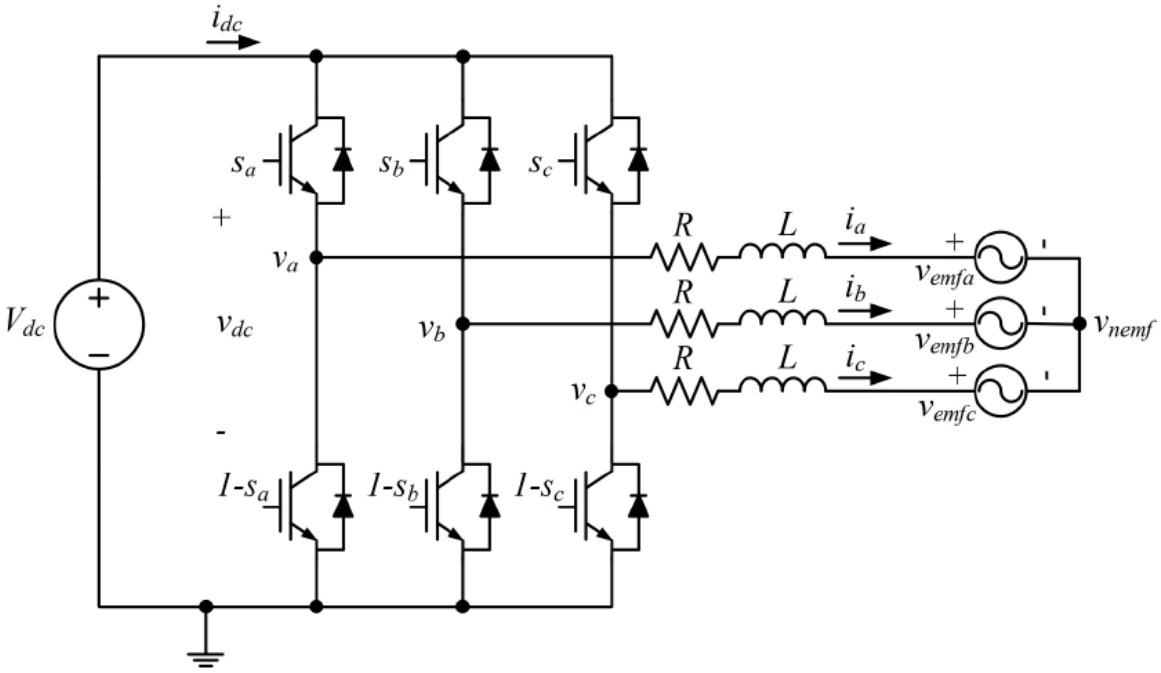

Figure 2.22. A three-phase voltage source inverter.

1. Switching model:

$$\vec{v}_{abc} = \vec{S}_{ph}.V_{dc}$$

$$i_{dc} = \vec{S}_{ph}^{T}.\vec{i}_{dc}$$

2. State space model: Differential equation for i_{abc}

$$\vec{v}_{ph} = R.\vec{i}_{ph} + L\frac{d}{dt}\vec{i}_{ph} + \vec{v}_{emfph} + \vec{v}_{nemf}$$

$$\frac{d}{dt}\vec{i}_{ph} = \frac{1}{L}\vec{v}_{ph} - \frac{R}{L}\vec{i}_{ph} - \frac{1}{L}\vec{v}_{emfph} - \frac{1}{L}\vec{v}_{nemf}$$

$$\vec{v}_{nemf} = \frac{1}{3}\sum_{k=a,b,c}\vec{v}_{phk} - \frac{1}{3}\sum_{k=a,b,c}\vec{v}_{emfk}$$

$$\frac{d}{dt}\vec{i}_{ph} = \frac{1}{L}\vec{v}_{ph} - \frac{R}{L}\vec{i}_{ph} - \frac{1}{L}\vec{v}_{emfph} - \frac{1}{3L}\sum_{k=a,b,c}\vec{v}_{phk} + \frac{1}{3L}\sum_{k=a,b,c}\vec{v}_{emfk}$$

3. Switching model of the system in abc coordinates:

$$\frac{d}{dt}\vec{\imath}_{ph} = \frac{1}{L}\vec{S}_{ph}.v_{dc} - \frac{R}{L}\vec{\imath}_{ph} - \frac{1}{L}\vec{v}_{emfph} - \frac{1}{3L}\sum_{k=a,b,c}\vec{S}_{phk}v_{dc} + \frac{1}{3L}\sum_{k=a,b,c}\vec{v}_{emfk}$$

$$i_{dc} = \vec{S}_{ph}^{T}.\vec{\imath}_{ph}$$

4. Applying average operator to switching model of the system:

$$\frac{1}{T}\int_{t-T}^{t}\frac{d}{dt}\vec{\imath}_{ph}(\tau)\,d\tau = \frac{1}{T}\int_{t-T}^{t}(\frac{1}{L}\vec{S}_{ph}(\tau).v_{dc}(\tau) - \frac{R}{L}\vec{\imath}_{ph}(\tau) - \frac{1}{3L}\sum_{k=a,b,c}\vec{S}_{phk}(\tau)v_{dc}(\tau) + \frac{1}{3L}\sum_{k=a,b,c}\vec{v}_{emfk})d\tau$$

5. Average model from above in abc coordinates:

$$\frac{d}{dt}\bar{\imath}_{ph} = \frac{1}{L}d_{ph}\bar{v}_{dc} - \frac{R}{L}\bar{\imath}_{ph} - \frac{1}{L}\vec{v}_{emfph} - \frac{1}{3L}\sum_{k=a,b,c}d_{phk}\bar{v}_{dc} + \frac{1}{3L}\sum_{k=a,b,c}\vec{v}_{emfk}$$

$$i_{dc} = \vec{d}_{ph}^{T}.\vec{\imath}_{abc}$$

6. Merging terms:

$$\frac{1}{L}d_{ph}\bar{v}_{dc} - \frac{1}{3L}\sum_{k=a,b,c}d_{kph}\bar{v}_{dc} = \frac{1}{3L}\begin{bmatrix}2 & -1 & -1\\ -1 & 2 & -1\\ -1 & -1 & 2\end{bmatrix}d_{ph}\bar{v}_{dc}$$

$$-\frac{1}{L}v_{emfph} + \frac{1}{3L}\sum_{k=a,b,c}v_{emfk} = \frac{1}{3L}\begin{bmatrix}-2 & 1 & 1\\ 1 & -2 & 1\\ 1 & 1 & -2\end{bmatrix}\bar{v}_{emfph}$$

$$\frac{d}{dt}\bar{\imath}_{ph} = -\frac{R}{L}\bar{\imath}_{ph} + \frac{1}{3L}\begin{bmatrix}2 & -1 & -1\\ -1 & 2 & -1\\ -1 & -1 & 2\end{bmatrix}d_{ph}\bar{v}_{dc} + \frac{1}{3L}\begin{bmatrix}-2 & 1 & 1\\ 1 & -2 & 1\\ 1 & 1 & -2\end{bmatrix}\bar{v}_{emfph}$$

7. Average model in abc coordinates in canonical form:

$$\frac{d}{dt}\begin{bmatrix}\bar{\imath}_a\\ \bar{\imath}_b\\ \bar{\imath}_c\end{bmatrix} = -\frac{R}{L}\begin{bmatrix}\bar{\imath}_a\\ \bar{\imath}_b\\ \bar{\imath}_c\end{bmatrix} + \frac{1}{3L}\begin{bmatrix}2 & -1 & -1\\ -1 & 2 & -1\\ -1 & -1 & 2\end{bmatrix}\begin{bmatrix}d_a\\ d_b\\ d_b\end{bmatrix}\bar{v}_{dc} + \frac{1}{3L}\begin{bmatrix}-2 & 1 & 1\\ 1 & -2 & 1\\ 1 & 1 & -2\end{bmatrix}\begin{bmatrix}\bar{v}_{emfa}\\ \bar{v}_{emfb}\\ \bar{v}_{emfc}\end{bmatrix}$$

$$i_{dc} = [d_a \quad d_b \quad d_c]^{T}.\begin{bmatrix}\bar{\imath}_a\\ \bar{\imath}_b\\ \bar{\imath}_c\end{bmatrix}$$

8. Coordinate transformation from abc to $\alpha\beta\gamma$ coordinates:

$$\bar{X}_{abc} = T_s^{-1}.\bar{X}_{\alpha\beta\gamma}$$

$$T_s^{-1}\frac{d}{dt}\bar{\imath}_{\alpha\beta\gamma ph} = -\frac{R}{L}T_s^{-1}\bar{\imath}_{\alpha\beta\gamma ph} + \frac{1}{3L}\begin{bmatrix}2 & -1 & -1\\ -1 & 2 & -1\\ -1 & -1 & 2\end{bmatrix}T_s^{-1}d_{\alpha\beta\gamma ph}\bar{v}_{dc} + \frac{1}{3L}\begin{bmatrix}-2 & 1 & 1\\ 1 & -2 & 1\\ 1 & 1 & -2\end{bmatrix}T_s^{-1}\bar{v}_{emf\alpha\beta\gamma}$$

$$T_s \times T_s^{-1}\frac{d}{dt}\bar{\imath}_{\alpha\beta\gamma ph} = -\frac{R}{L}T_s \times T_s^{-1}\bar{\imath}_{\alpha\beta\gamma ph} + \frac{1}{3L}T_s\begin{bmatrix}2 & -1 & -1\\ -1 & 2 & -1\\ -1 & -1 & 2\end{bmatrix}T_s^{-1}d_{\alpha\beta\gamma ph}\bar{v}_{dc} + \frac{1}{3L}T_s\begin{bmatrix}-2 & 1 & 1\\ 1 & -2 & 1\\ 1 & 1 & -2\end{bmatrix}T_s^{-1}\bar{v}_{emf\alpha\beta\gamma}$$

$$T_s\begin{bmatrix}2 & -1 & -1\\ -1 & 2 & -1\\ -1 & -1 & 2\end{bmatrix}T_s^{-1} = \begin{bmatrix}3 & 0 & 0\\ 0 & 3 & 0\\ 0 & 0 & 0\end{bmatrix}$$

$$\frac{d}{dt}\bar{\imath}_{\alpha\beta\gamma ph} = -\frac{R}{L}\bar{\imath}_{\alpha\beta\gamma ph} + \frac{1}{L}d_{\alpha\beta\gamma ph}\bar{v}_{dc} - \frac{1}{L}\bar{v}_{emf\alpha\beta\gamma}$$

$$i_{dc} = d^T_{\alpha\beta\gamma ph}.\bar{\imath}_{\alpha\beta\gamma ph}$$

9. Average model in $\alpha\beta\gamma$ coordinates in canonical form:

$$\frac{d}{dt}\begin{bmatrix}\bar{\imath}_{\alpha ph}\\ \bar{\imath}_{\beta ph}\\ \bar{\imath}_{\gamma ph}\end{bmatrix} = -\frac{R}{L}\begin{bmatrix}\bar{\imath}_{\alpha ph}\\ \bar{\imath}_{\beta ph}\\ \bar{\imath}_{\gamma ph}\end{bmatrix} + \frac{\bar{v}_{dc}}{L}\begin{bmatrix}d_{\alpha ph}\\ d_{\beta ph}\\ d_{\gamma ph}\end{bmatrix} - \frac{1}{L}\begin{bmatrix}\bar{v}_{emf\alpha}\\ \bar{v}_{emf\beta}\\ \bar{v}_{emf\gamma}\end{bmatrix}$$

$$i_{dc} = [d_{\alpha ph} \quad d_{\beta ph} \quad d_{\gamma ph}]^T.\begin{bmatrix}\bar{\imath}_{\alpha ph}\\ \bar{\imath}_{\beta ph}\\ \bar{\imath}_{\gamma ph}\end{bmatrix}$$

10. Coordinate transformation from abc to $dq0$ coordinates:

$$\frac{d(T_s^{-1}\bar{\imath}_{dq0ph})}{dt} = -\frac{R}{L}T_s^{-1}\bar{\imath}_{dq0ph} + \frac{1}{3L}\begin{bmatrix}2 & -1 & -1\\ -1 & 2 & -1\\ -1 & -1 & 2\end{bmatrix}T_s^{-1}d_{dq0ph}\bar{v}_{dc} - \frac{1}{3L}\begin{bmatrix}2 & -1 & -1\\ -1 & 2 & -1\\ -1 & -1 & 2\end{bmatrix}T_s^{-1}\bar{v}_{emfdq0}$$

$$\frac{d}{dt}\bar{\imath}_{dq0ph} = -T_s\frac{dT_s^{-1}}{dt}\bar{\imath}_{dq0ph} - \frac{R}{L}\bar{\imath}_{dq0ph} + \frac{1}{3L}T_s\begin{bmatrix}2 & -1 & -1\\ -1 & 2 & -1\\ -1 & -1 & 2\end{bmatrix}T_s^{-1}d_{dq0ph}\bar{v}_{dc} - \frac{1}{3L}T_s\begin{bmatrix}2 & -1 & -1\\ -1 & 2 & -1\\ -1 & -1 & 2\end{bmatrix}T_s^{-1}\bar{v}_{emfdq0}$$

11. Solution:

$$T_s \frac{dT_s^{-1}}{dt} = \begin{bmatrix} 0 & -\omega & 0 \\ \omega & 0 & 0 \\ 0 & 0 & 0 \end{bmatrix}$$

$$T_s \begin{bmatrix} 2 & -1 & -1 \\ -1 & 2 & -1 \\ -1 & -1 & 2 \end{bmatrix} T_s^{-1} = \begin{bmatrix} 3 & 0 & 0 \\ 0 & 3 & 0 \\ 0 & 0 & 0 \end{bmatrix}$$

12. Average model from above in $dq0$ coordinates:

$$\frac{d}{dt}\bar{\imath}_{dq0ph} = -\begin{bmatrix} 0 & -\omega & 0 \\ \omega & 0 & 0 \\ 0 & 0 & 0 \end{bmatrix}\bar{\imath}_{dq0ph} - \frac{R}{L}\bar{\imath}_{dq0ph} + \frac{1}{3L}d_{dq0ph}\bar{v}_{dc} - \frac{1}{L}\bar{v}_{emfdq0}$$

$$i_{dc} = d_{dq0ph}^{T}.\bar{\imath}_{dq0ph}$$

13. Average model in $dq0ph$ coordinates in canonical form:

$$\frac{d}{dt}\begin{bmatrix} \bar{\imath}_{dph} \\ \bar{\imath}_{qph} \\ \bar{\imath}_{0ph} \end{bmatrix} = -\begin{bmatrix} 0 & -\omega & 0 \\ \omega & 0 & 0 \\ 0 & 0 & 0 \end{bmatrix}\begin{bmatrix} \bar{\imath}_{dph} \\ \bar{\imath}_{qph} \\ \bar{\imath}_{0ph} \end{bmatrix} - \frac{R}{L}\begin{bmatrix} \bar{\imath}_{dph} \\ \bar{\imath}_{qph} \\ \bar{\imath}_{0ph} \end{bmatrix} + \frac{\bar{v}_{dc}}{L}\begin{bmatrix} d_{dph} \\ d_{qph} \\ d_{0ph} \end{bmatrix} - \frac{1}{L}\begin{bmatrix} \bar{v}_{emfd} \\ \bar{v}_{emfq} \\ \bar{v}_{emf0} \end{bmatrix} \quad (2.29)$$

$$i_{dc} = [d_{dph} \quad d_{qph} \quad d_{0ph}]^{T}.\begin{bmatrix} \bar{\imath}_{dph} \\ \bar{\imath}_{qph} \\ \bar{\imath}_{0ph} \end{bmatrix} \quad (2.30)$$

14. Using equation of average model in $dq0$ coordinates, the equivalent circuit:

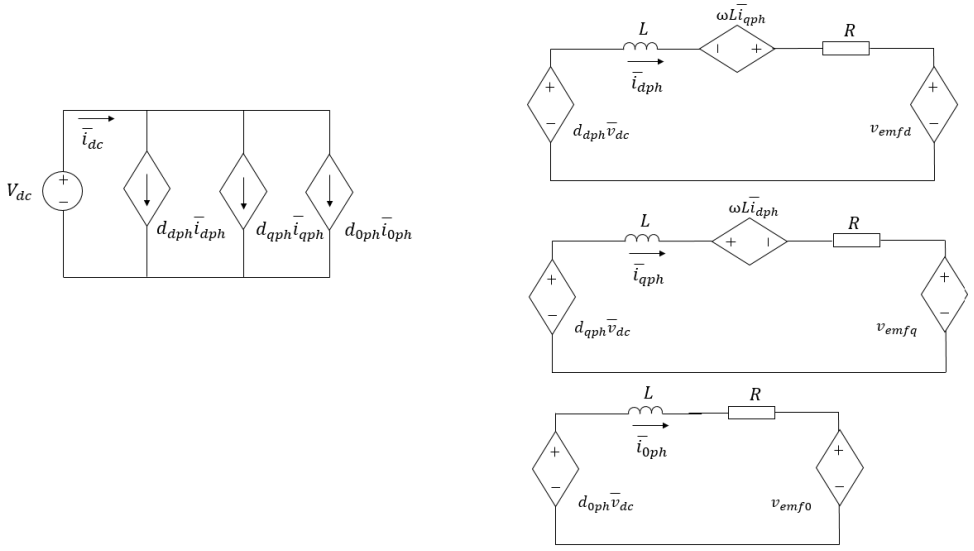

Figure 2.23 Equivalent circuit of average model in dq0 frame.

System control modeling

Average model of the converters in the dq reference frame is presented in Figure 2.23

Average model in dq coordinates in canonical form is shown in equations 2.31 and 2.32.

$$\frac{d}{dt}\begin{bmatrix}\bar{\imath}_d\\ \bar{\imath}_q\\ \bar{\imath}_0\end{bmatrix} = \frac{\bar{V}_{dc}}{L}\begin{bmatrix}1 & 0 & 0\\ 0 & 1 & 0\\ 0 & 0 & 0\end{bmatrix}\begin{bmatrix}\bar{d}_d\\ \bar{d}_q\\ \bar{d}_0\end{bmatrix} - \frac{R}{L}\begin{bmatrix}\bar{\imath}_d\\ \bar{\imath}_q\\ \bar{\imath}_0\end{bmatrix} - \frac{1}{L}\begin{bmatrix}1 & 0 & 1\\ 0 & 1 & 0\\ 0 & 0 & 0\end{bmatrix}\begin{bmatrix}\bar{v}_{emfd}\\ \bar{v}_{emfq}\\ \bar{v}_{emf0}\end{bmatrix} - \begin{bmatrix}0 & -\omega_g & 0\\ \omega_g & 0 & 0\\ 0 & 0 & 0\end{bmatrix}\begin{bmatrix}\bar{\imath}_d\\ \bar{\imath}_q\\ \bar{\imath}_0\end{bmatrix} \tag{2.31}$$

$$\bar{\imath}_{dc} = \begin{bmatrix}\bar{d}_d & \bar{d}_q & \bar{d}_0\end{bmatrix}^T\begin{bmatrix}\bar{\imath}_d\\ \bar{\imath}_q\\ \bar{\imath}_0\end{bmatrix} \tag{2.32}$$

$$L\frac{d}{dt}\bar{\imath}_{dph} = -R\bar{\imath}_{dph} + V_{dc}\bar{d}_{dph} - V_{emfdph} + \omega_g L\bar{\imath}_{qph} \tag{2.33}$$

$$L\frac{d}{dt}\bar{\imath}_{qph} = -R\bar{\imath}_{qph} + V_{dc}\bar{d}_{qph} - V_{emfqph} + \omega_g L\bar{\imath}_{dph} \tag{2.34}$$

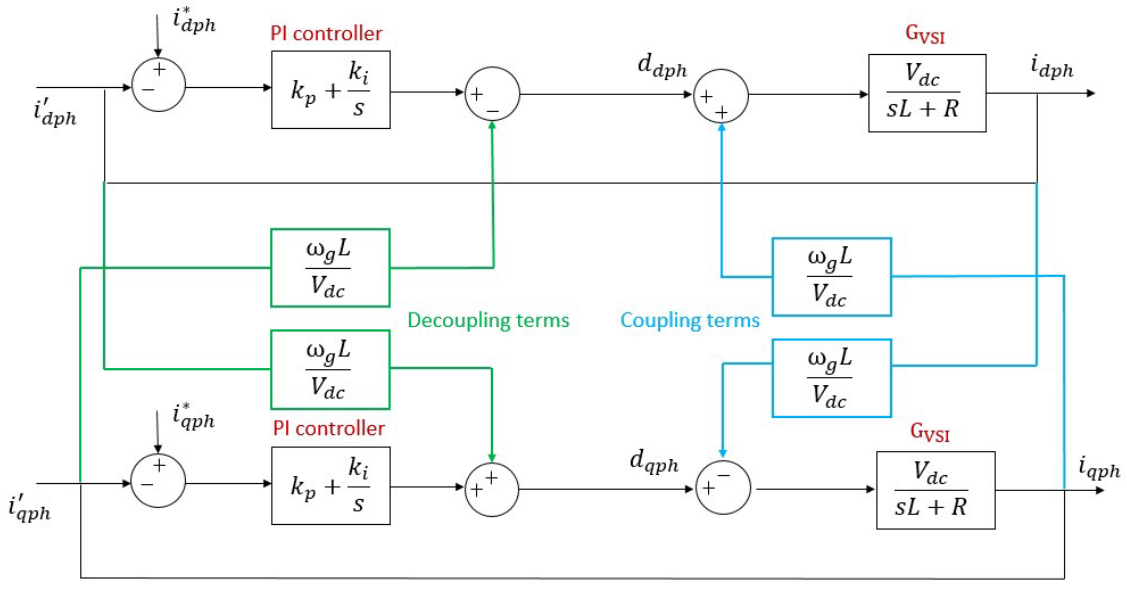

Figure 2.24 System control block diagram with decoupling terms

RMS value of line-to-line grid voltage is 208V in sinusoidal form. To convert voltage from abc frame to dq frame, orthoganal transformation matrix was used as shown in equation 2.35.

$$T_{dq0/abc} = \begin{bmatrix} T_d \\ T_q \\ T_0 \end{bmatrix} = \frac{2}{3} \begin{bmatrix} \cos\theta & \cos(\theta - \frac{2\pi}{3}) & \cos(\theta + \frac{2\pi}{3}) \\ -\sin\theta & -\sin(\theta - \frac{2\pi}{3}) & -\sin(\theta + \frac{2\pi}{3}) \\ \frac{1}{2} & \frac{1}{2} & \frac{1}{2} \end{bmatrix} \begin{bmatrix} T_a \\ T_b \\ T_c \end{bmatrix} \quad (2.35)$$

$V_{emfdph} = 169V$, $V_{emfqph} = 0$, coupling terms can be eliminated by following decoupling terms:

$$d^*_{dph} = d_{dph} - \frac{\omega_g L i_q}{V_{dc}} \quad (2.36)$$

$$d^*_{qph} = d_{qph} - \frac{\omega_g L i_d}{V_{dc}} \quad (2.37)$$

The physical model of the circuit after eliminating decoupling terms becomes:

$$L\frac{d}{dt}\bar{\imath}_{dph} = -R\bar{\imath}_{dph} + V_{dc}\bar{d}_{dph} \quad (2.38)$$

$$L\frac{d}{dt}\bar{\imath}_{qph} = -R\bar{\imath}_{qph} + V_{dc}\bar{d}_{qph} \quad (2.39)$$

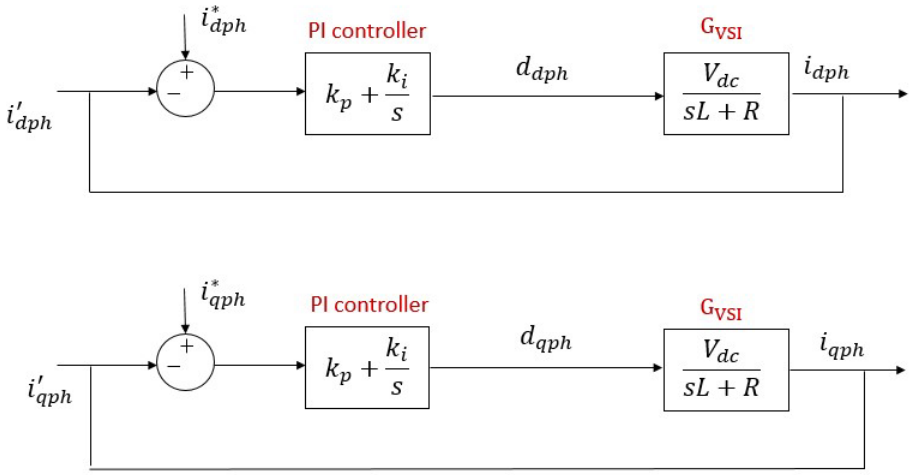

Figure 2.25 System control block diagram after eliminating decoupling terms.

Transfer function for decoupled voltage source inverter mode is determined by following equation:

$$G_{VSI} = \frac{i_{dph(s)}}{d_{dph(s)}} = \frac{V_{dc}}{sL + R} \quad (2.40)$$

Open-loop transfer function of the system with PI controller and voltage source inverter:

$$G_{op}(s) = (k_{ip} + \frac{k_{ii}}{s}) \cdot \frac{V_{dc}}{sL + R} \tag{2.41}$$

The cut-off frequency ω_c was set as 1/200 of switching frequency, and phase margin as 65. The value of $k_{ip} = 8.2417 \cdot 10^{-4}$ and $k_{ii} = 0.2770$ were calculated from the following equations:

$$\left|G_{op}(j\omega_c)\right| = 1 \tag{2.42}$$

$$\angle G_{op}(j\omega_c) = -\pi\frac{180 - \Phi_m}{180} \tag{2.43}$$

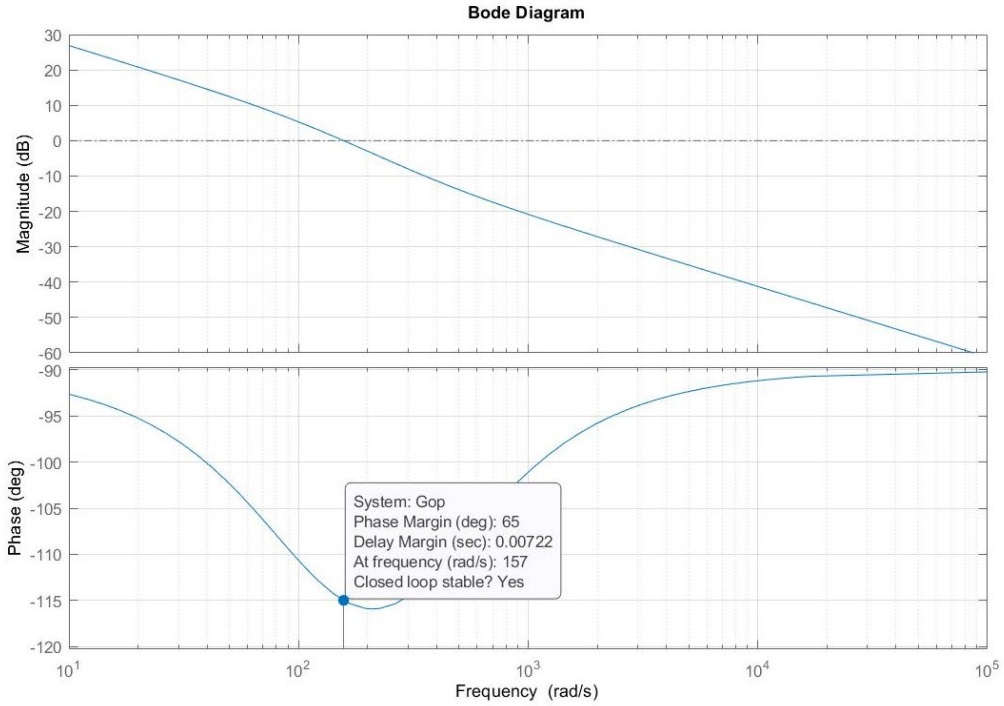

Figure 2.26 Bode plot of open-loop transfer function

From the bode plot of open-loop transfer function, it can be determined that the system is stable with desired phase margin of 65.

Pulse width modulation (PWM):

Pulse width modulation is one of the most widely utilized strategies for controlling the AC output of power electronic converters. In simplest terms, PWM is a way to control analog devices with a digital output. PWM varies the duty cycle of converter switches at a high switching frequency to achieve a target average low-

frequency output voltage or current [36]. It controls the amount of power given to a device by switching the on and off phases of a digital signal and hence, varying the duty cycle or the on-phase width. The primary aim of PWM is to generate switching pulses for the inverter to produce an output voltage with desired amplitude and frequency [37]. Various PWM techniques have been developed which can be mainly classified into three categories – programmed, carrier-based and space vector PWM [37]. Classification of PWM techniques is depicted in figure 2.27. There are various performance criterions that could be used to evaluate these PWM techniques. For instance, the assessment of the harmonics included in output voltage is vital in determining the quality of output voltage since fewer harmonics in output voltage means that the output voltage approaches a pure sinusoidal AC [36].

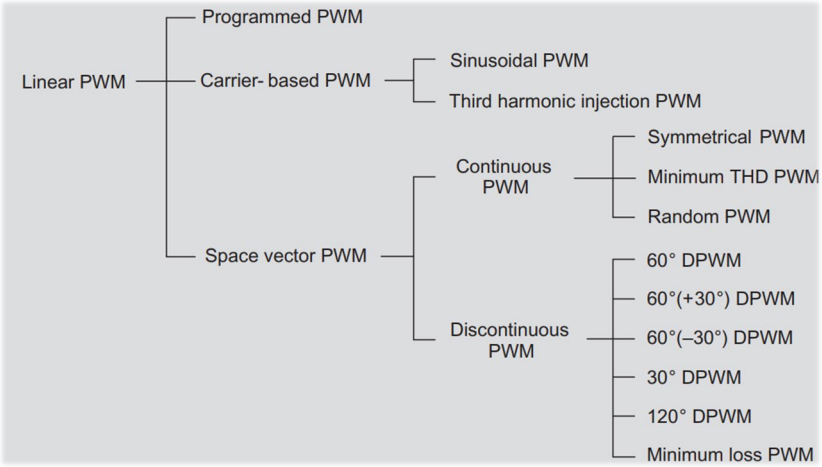

Figure 2.27 Classifications of pulse width modulation techniques [37].

Sinusoidal PWM: This is the most commonly used carrier-based PWM technique which utilizes a sinusoidal AC voltage reference to modulate a high frequency triangular carrier wave [38]. It has the advantage of having a constant switching frequency due to which calculating switching losses is possible [37]. Furthermore, implementing a low-pass filter is easier in sinusoidal PWM due to well-defined harmonic characteristics [37]. Therefore, for this project it was decided to utilize sinusoidal PWM technique. Switching states for each pole are determined using below mentioned rules [37] –

i. If reference voltage is greater than triangular carrier then upper switch is turned on, i.e. pole voltage = $V_{dc}/2$.

ii. If reference voltage is less than triangular carrier then lower switch is turned on, i.e. pole voltage = $-V_{dc}/2$.

Obtained waveforms at rated solar radiation and wind speed:

The Simulink model of the control for voltage source inverter implemented in the proposed system is shown in figure 2.28. The current reference (id_ref) was obtained using the bus voltage. This current reference was compared to the current value from the grid side in dq-frame to obtain reference signals (d_d and d_q). These signals were then converted to abc-frame to implement sinusoidal pulse width modulation technique and obtain the switching signals of the VSI.

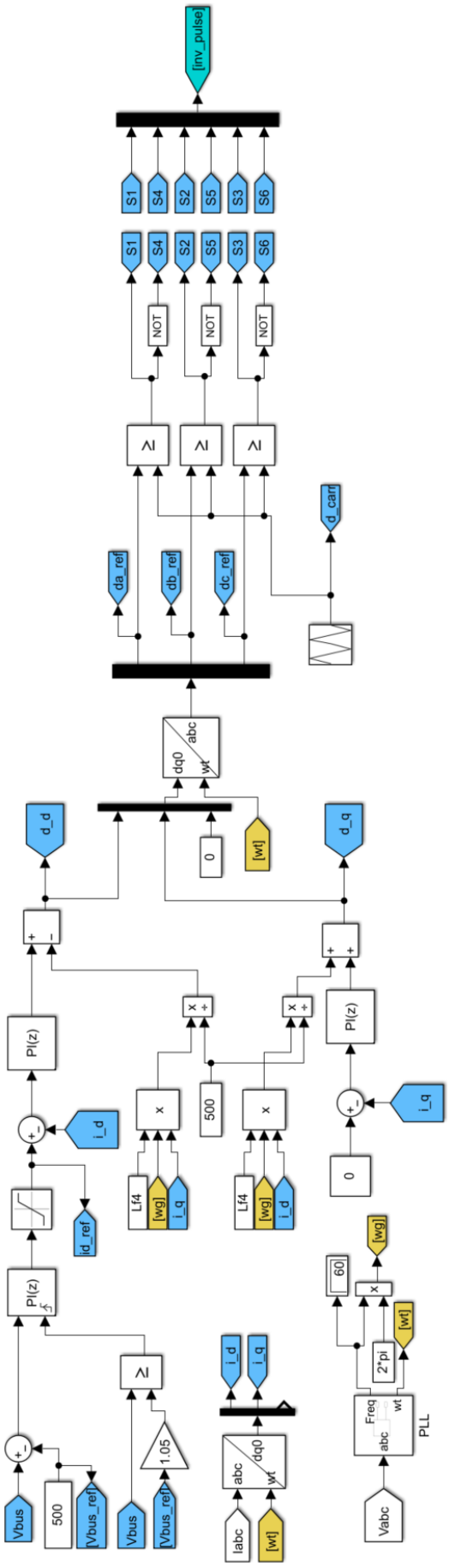

Figure 2.28 VSI control

Obtained waveforms of the gate, reference and carrier signals are depicted in figures 2.29a, 2.29b and 2.29c. The figures show that if reference voltage is greater than triangular carrier then upper switch is turned on and if reference voltage is lesser than triangular carrier then lower switch is turned on, as expected.

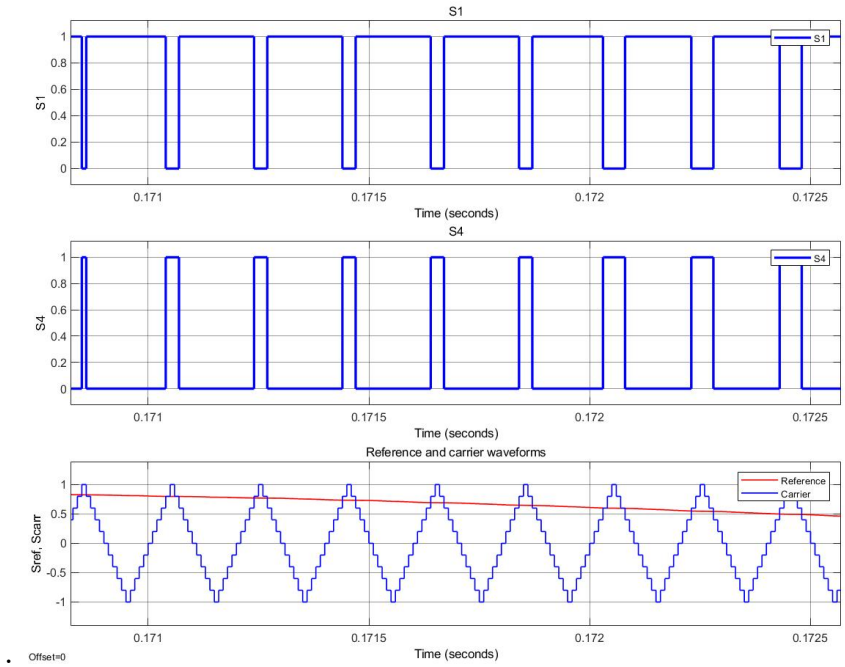

Figure 2.29a Gate signal of upper and lower switch; and reference and carrier waveforms: Leg 1

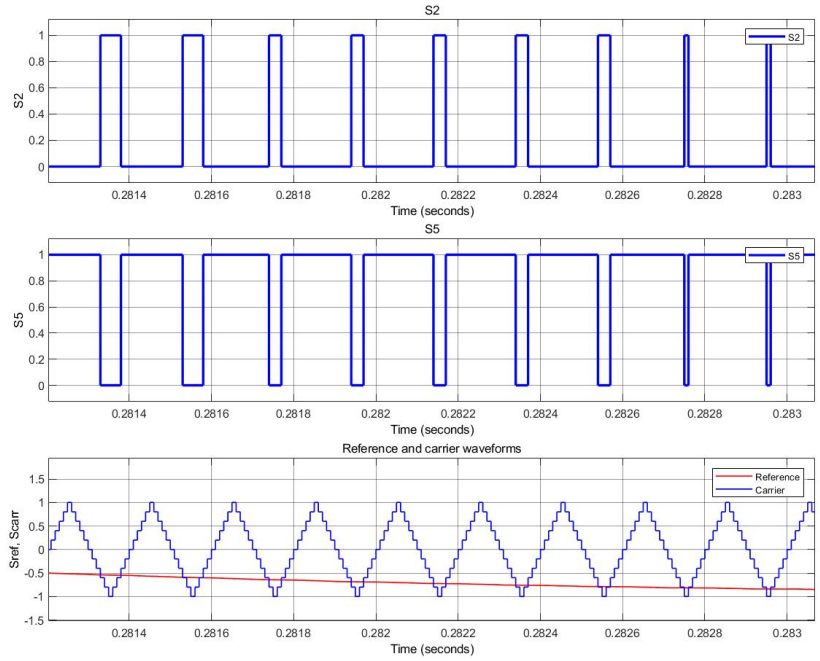

Figure 2.29b. Gate signal of upper and lower switch; and reference and carrier waveforms: Leg 2

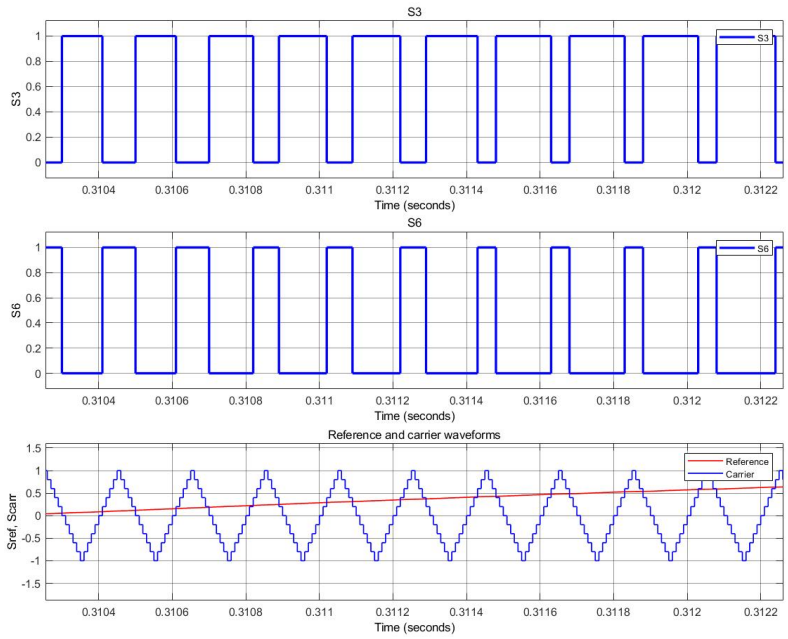

Figure 2.29c. Gate signal of upper and lower switch; and reference and carrier waveforms: Leg 3

Current, I_d = 74.8A. To obtain power factor 1, I_q value was set to 0 (figure 2.30). Duty cycles D_d and D_q vary between -1 and 1. The value of D_d was measured to be 0.82 and D_q to be 0.32 (figure 2.31).

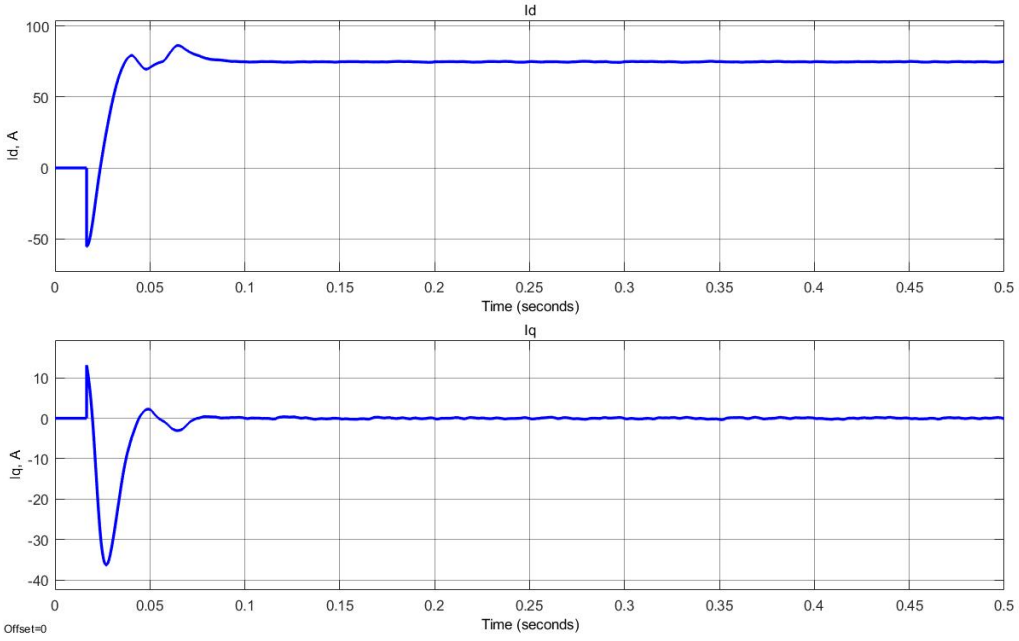

Figure 2.30 Current Id and Iq

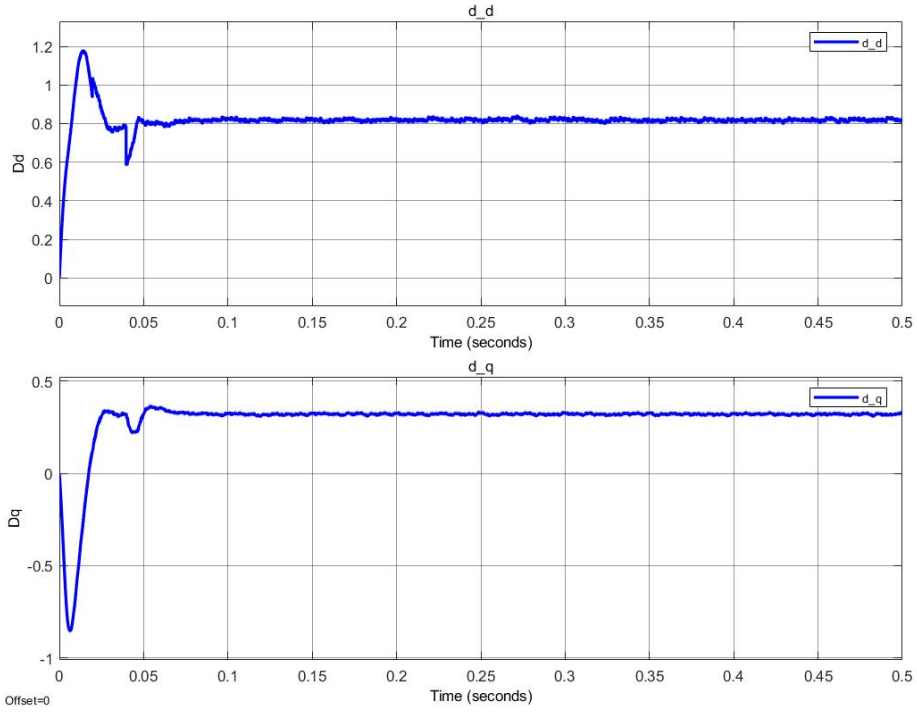

Figure 2.31 Duty cycle Dd and Dq

Output power obtained from wind turbine and solar panels was measured before and after boost converter. Since MPPT was not implemented for wind turbine, it was observed that the 12kW power generated by wind turbine was reduced to 10.6kW after boost converter (figure 2.32). On the other hand, due to implementation of MPPT for PV array, the power conversion ratio was close to 1 and the 12.72kW power out of the PV panels was reduced only to 12.65kW out of boost converter (figure 2.33). The maximum power out of system at rated conditions, i.e. solar irradiation of 1000 W/m^2 and wind speed of 14m/sec, was measured as 23.3kW (figure 2.34). After settling, the bus voltage of the system could be kept as 500V (figure 2.35).

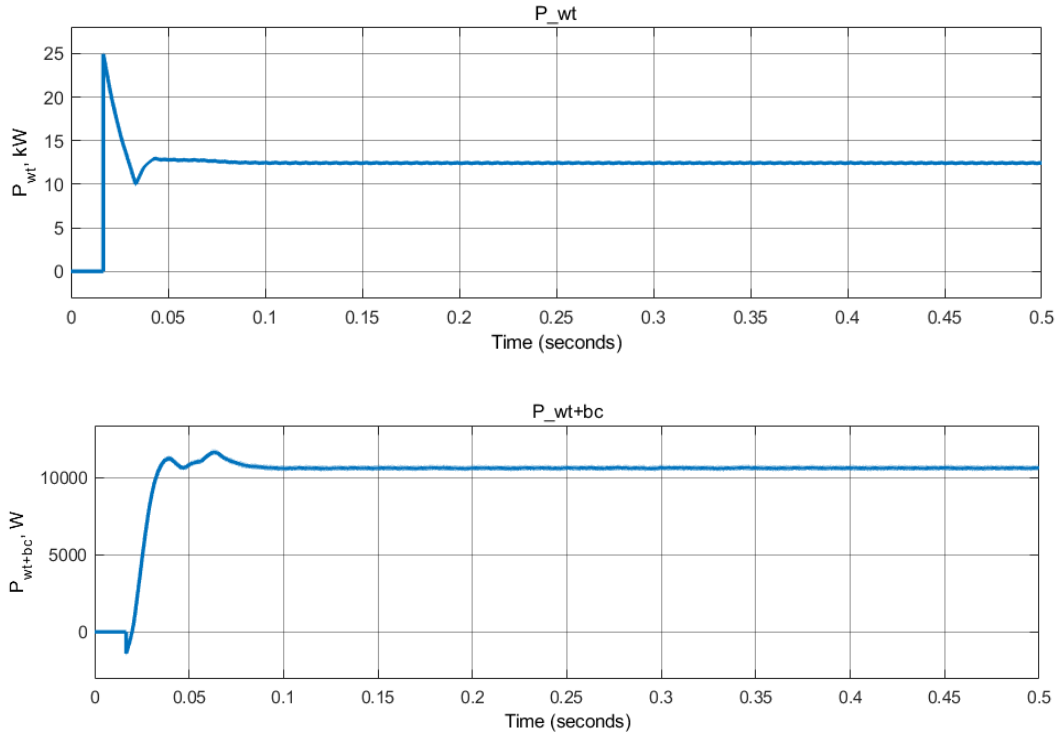

Figure 2.32 Power out of wind turbine before and after boost converter

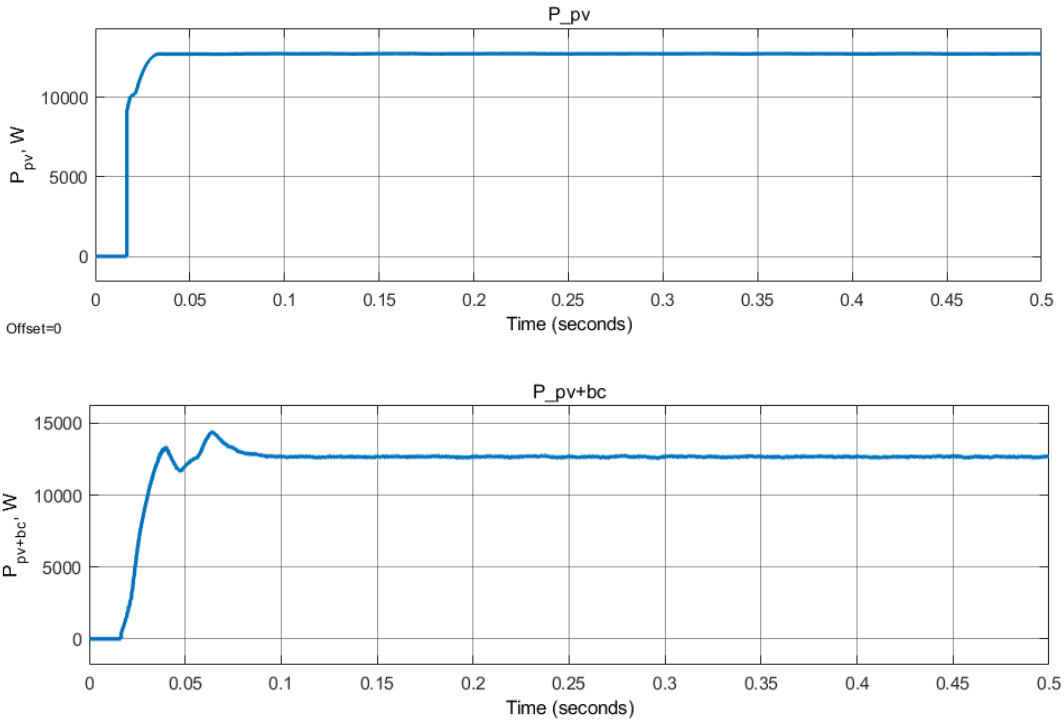

Figure 2.33 Power out of PV system before and after boost converter

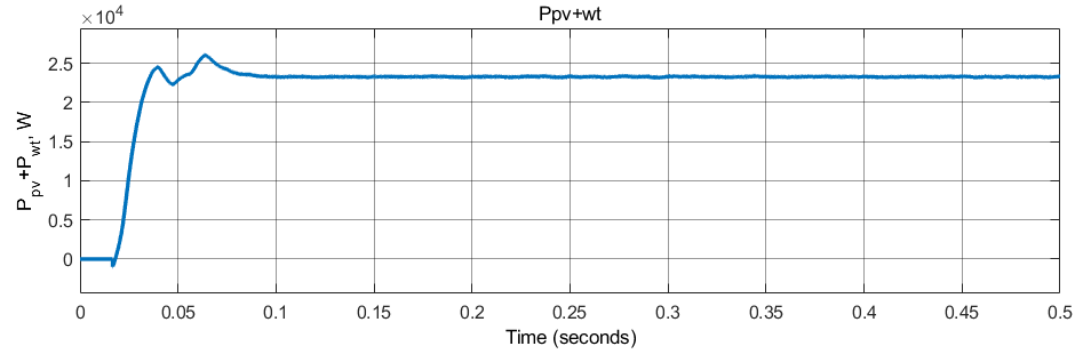

Figure 2.34 Power out PV+WT waveforms

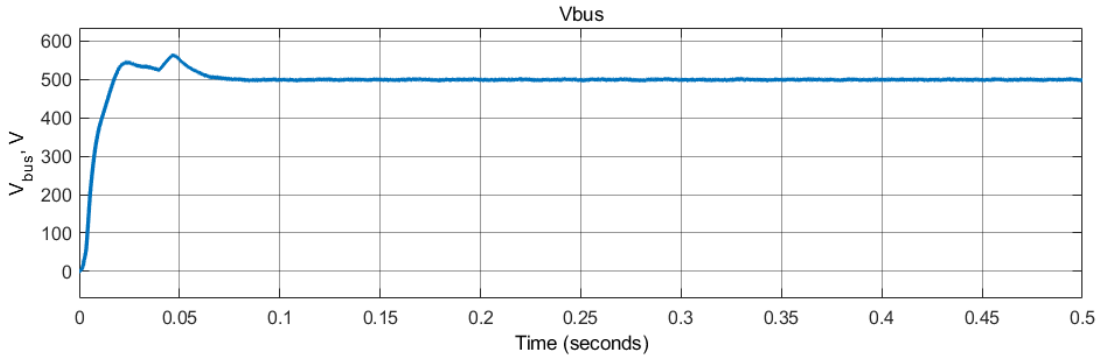

Figure 2.35 Bus voltage

Figure 2.36 shows the inverter voltage waveforms, which clearly depict that the unipolar switching sequence was obtained. This is in line with the theory that three phase system generally generate unipolar switching. Unipolar switching sequence is said to have formed when the output is switched from high to zero or from low to zero. The first graph in figure 2.36 shows the three-phase voltage of the grid which is a sinusoidal waveform with desired magnitude of 208V. The second and third graphs show the phase-a inverter voltage and its moving average respectively, and the fourth graph depicts the line to line voltage between phase-a and phase-b. Current waveforms are presented in figure 2.37, with the first graph showing the sinusoidal grid current and the second one shows the sinusoidal current waveform measured out of inverter before the implantation of L-filter.

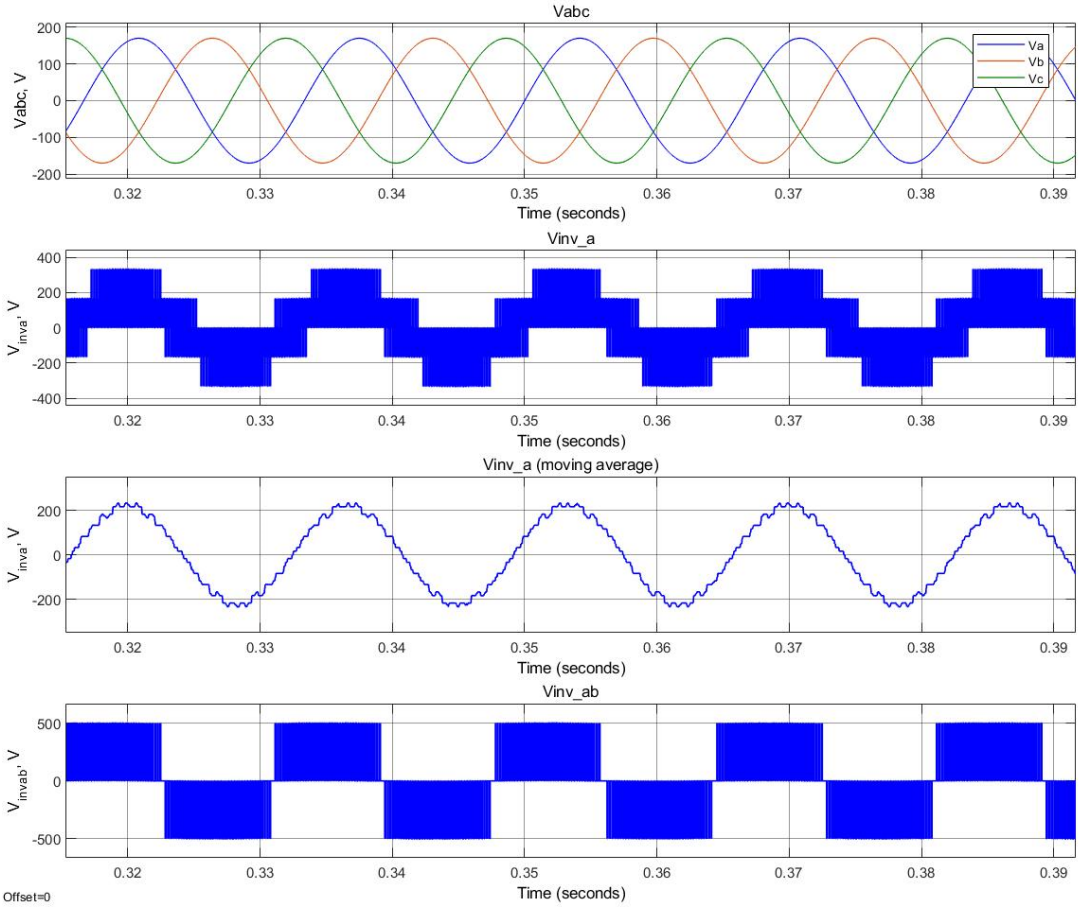

Figure 2.36. Voltage waveforms

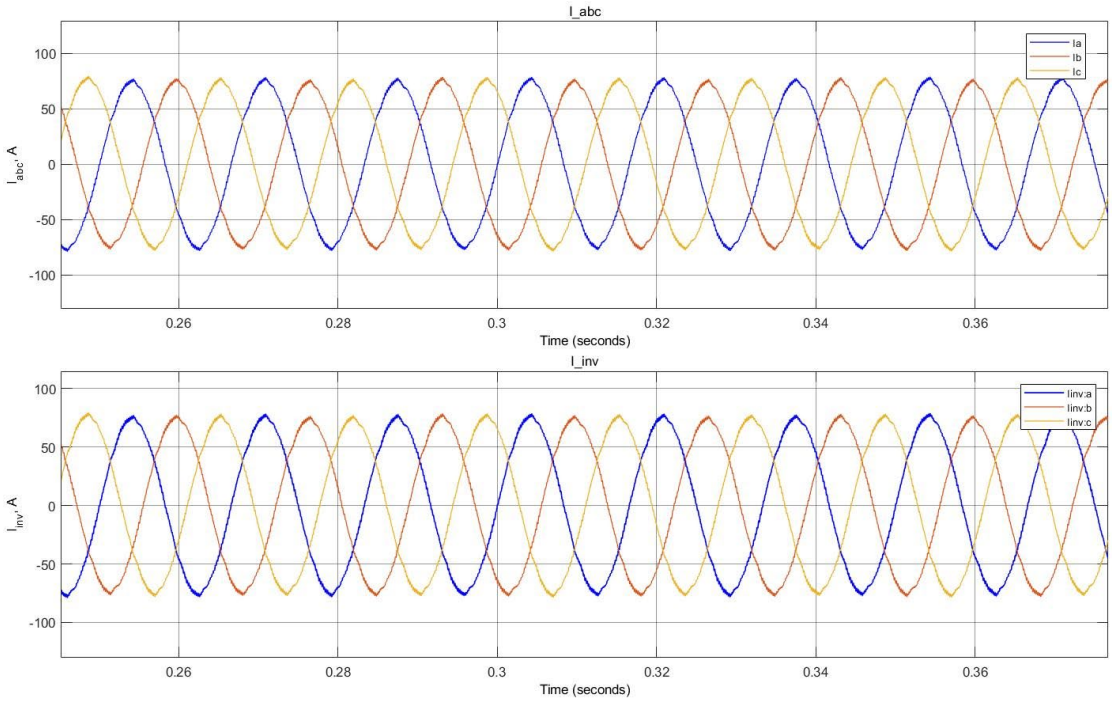

Figure 2.37. Current waveforms

THD of current waveforms was observed to be 2.36% and that of voltage is 82.81%. From the spectrum of the voltage and current out of the inverter, the dominant harmonics are centered around integer multiples of the switching frequency. So, the side band frequency is located around switching frequency of 5000Hz (Figure 2.38-2.39).

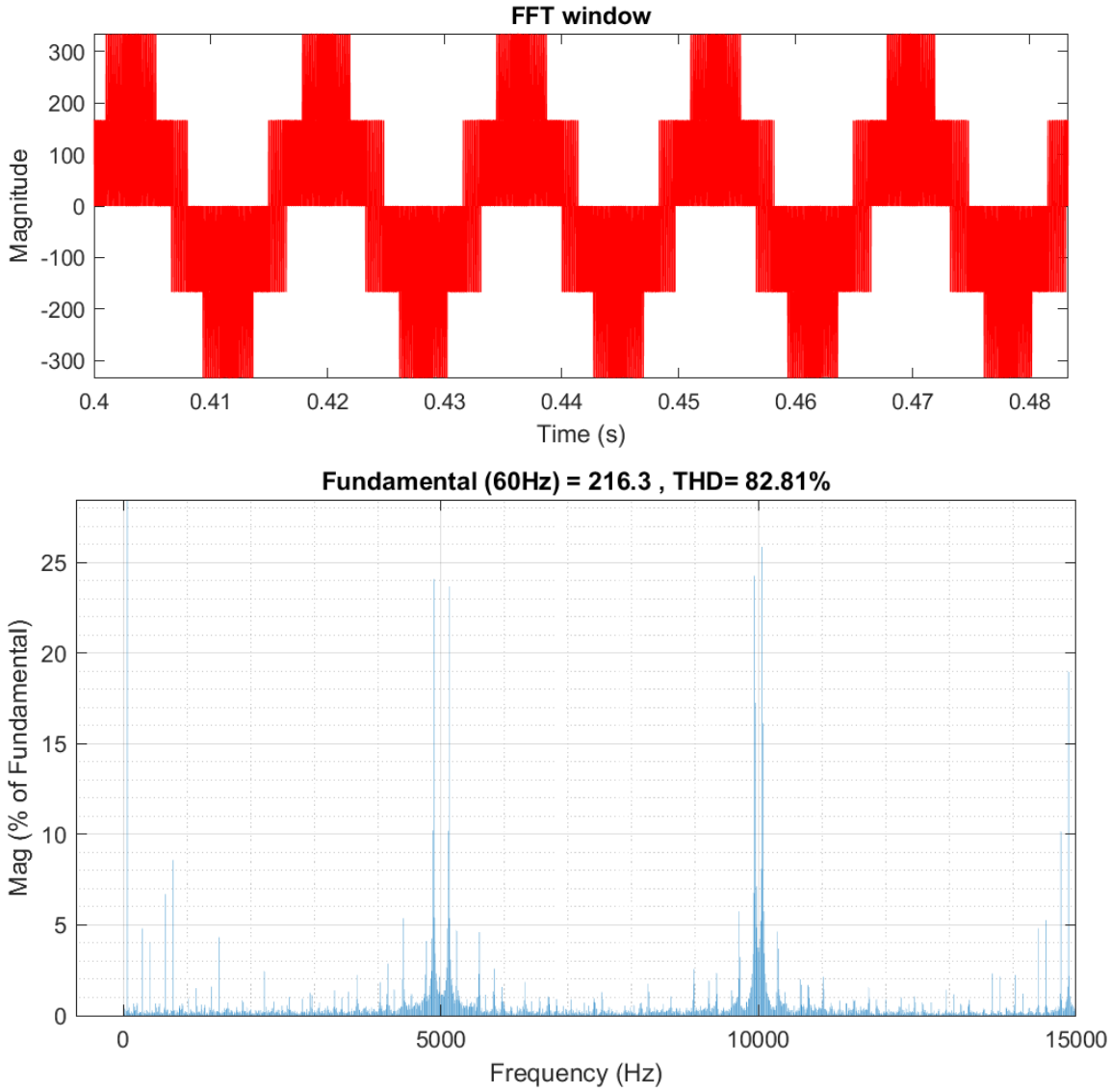

Figure 2.38. Spectrum of voltage outside inverter, phase A (Vinv_a)

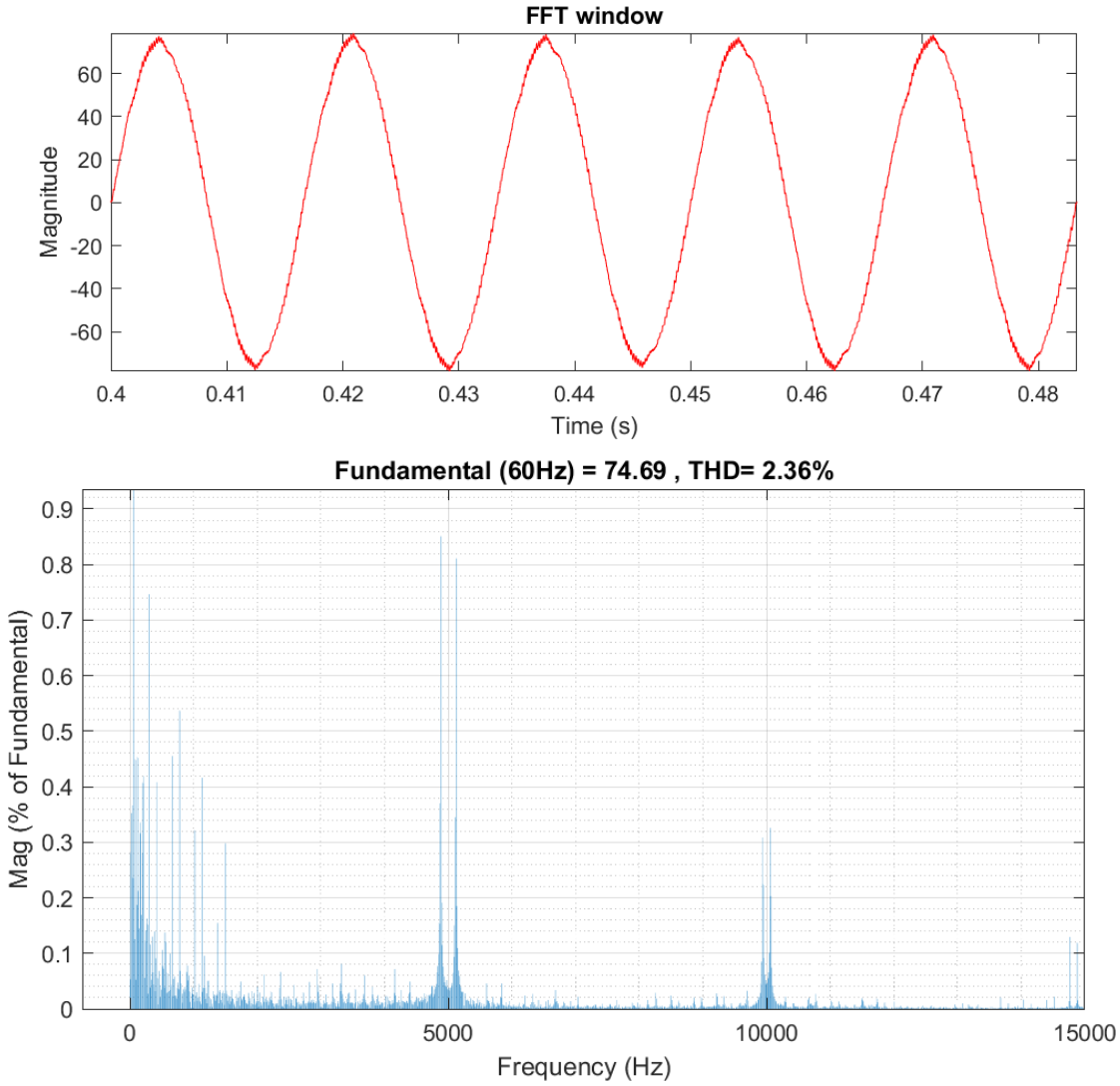

Figure 2.39. Spectrum of current outside inverter, phase A (I_inv_a)

The final MATLAB/SIMULINK model is presented in figure 2.40.

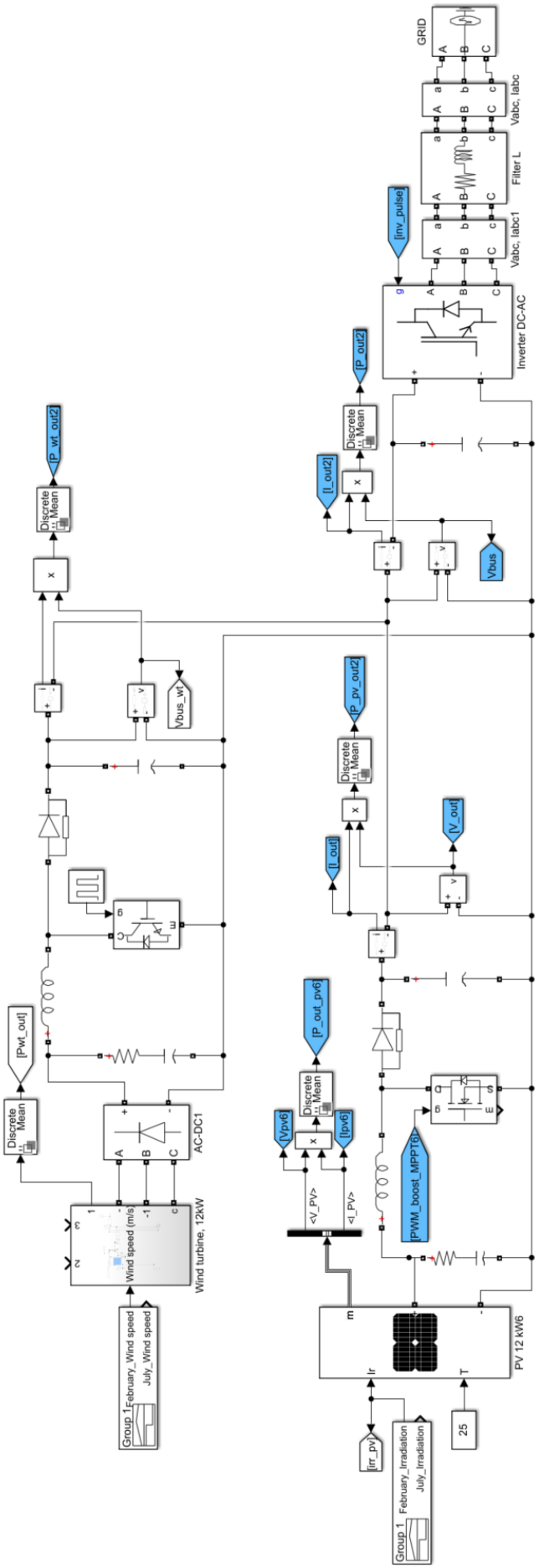

Figure 2.40. Complete PV-wind hybrid system

REFERENCES

[1] R.N. Clark, “Needs evaluation – Determining power need to meet the owner’s request,” in *Small wind planning and building successful installations, 1st* ed. Waltham, MA, USA: Academic Press, 2013, ch. *2*, pp. *29-37*.

[2] S. Heier, “Wind energy conversion systems,” in *Grid Integration of Wind Energy – Onshore and Offshore Conversion Systems, 3rd* ed. Wiesbaden, Germany: Vieweg+Teubner (in German), 2009, ch. *2*, pp. *31-116*.

[3] B. Wu, Y. Lang, N. Zargari, and S. Kouro, “Fundamentals of wind energy conversion system control,” in *Power Conversion and Control of Wind Energy Systems,* ed. Hoboken, NJ, USA: John Wiley & Sons Inc., 2011, ch. *2*, pp. *25-47*.

[4] V. Yaramasu, and B. Wu, “Basics of wind energy conversion systems (WECS),” in *Model Predictive Control of Wind Energy Conversion Systems,* ed. Hoboken, NJ, USA: John Wiley & Sons Inc., 2017, ch. *1*, pp. *1-60*.

[5] J. Dai, D. Liu, L. Wen, and X. Long, "Research on power coefficient of wind turbines based on SCADA data," ***Renewable Energy***, vol. 86, pp. 206-215, 2016, doi: http://dx.doi.org/10.1016/j.renene.2015.08.023.

[6] A. Soetedjo, A. Lomi, and Widodo Puji Mulayanto, "Modeling of wind energy system with MPPT control," ***Proceedings of the 2011 International Conference on Electrical Engineering and Informatics***, 2011, pp. 1-6, doi: 10.1109/ICEEI.2011.6021836.

[7] A. Kusiak, H. Zheng, and Z. Song, "Models for monitoring wind farm power," ***Renewable Energy***, vol. 34, no. 3, pp. 583-590, 2009, doi: https://doi.org/10.1016/j.renene.2008.05.032.

[8] S. Masri, and P. W. Chan, "Design and development of a DC-DC boost converter with constant output voltage," ***2010 International Conference on Intelligent and Advanced Systems***, 2010, pp. 1-4, doi: 10.1109/ICIAS.2010.5716257.

[9] V. Sohoni, S.C. Gupta, and R.K. Nema, "A critical review of wind turbine power curve modelling techniques and their applications in wind-based

energy systems," ***Journal of Energy (Hindawi)***, vol. 2016, pp. 1-18, 2016, doi: https://doi.org/10.1155/2016/8519785.

[10] X. Yang, X. Gong and W. Qiao, "Mechanical sensorless maximum power tracking control for direct-drive PMSG wind turbines," 2010 IEEE Energy Conversion Congress and Exposition, 2010, pp. 4091-4098, doi: 10.1109/ECCE.2010.5617749.

[11] C.N. Wang, W.C. Lin, and X.K. Le, "Modelling of a PMSG wind turbine with autonomous control," ***Journal of Energy (Hindawi)***, vol. 2014, pp. 1-9, 2014, doi: http://dx.doi.org/10.1155/2014/856173

[12] R. Melicio, V.M.F. Mendes, and J.P.S. Catalao, "Wind turbines with permanent magnet synchronous generator and full-power converters: Modelling, control and simulation," in *Wind Turbines,* Dr. Ibrahim Al-Bahadly, ed, InTech, 2011, ch. *20*, pp. *465-494*.

[13] A. Jain, S. Shankar, and V. Vanitha, "Power generation using permanent magnet synchronous generator (PMSG) based variable speed wind energy conversion system (WECS): An overview," ***Journal of Green Engineering***, vol. 7, no. 4, pp. 477-504, 2018, doi: 10.13052/jge1904-4720.742.

[14] S.M.M. Hasan, and A.H.M.D. Shatil, "Design and comparison of grid connected permanent magnet synchronous generator non-salient pole and salient pole rotor wind turbine," ***AIUB Journal of Science and Engineering***, vol. 20, no. 2, pp. 40-46, 2021.

[15] S.R. Wenham, M.A. Green, M.E. Watt, and R. Corkish, "The characteristics of sunlight," in *Applied Photovoltaics, 2nd* ed. London, UK: Earthscan, 2007, ch. *1*, pp. *3-29*.

[16] M.H. Taghvaee, M.A.M. Radzi, S.M. Moosavain, H. Hizam, and M.H. Marhaban, " A current and future study on non-isolated DC-DC converters for photovoltaic applications," ***Renewable and Sustainable Energy Reviews***, vol. 17, pp. 216-227, 2013, doi: http://dx.doi.org/10.1016/j.rser.2012.09.023.

[17] R.W. Erickson, and D. Maksimovic, "Principles of steady-state converter analysis," in *Fundamentals of Power Electronics, 3rd* ed. Cham, Switzerland: Springer, 2020, ch. *2*, pp. *15-42*.

[18] N.S, Nise, “Design via root locus,” in *Control Systems Engineering, 7th* ed. Hoboken, NJ, USA: John Wiley and Sons Inc., 2015, ch. *9*, pp. *449-524*.

[19] R. Alik, and A. Jusoh, "An enhanced P&O checking algorithm MPPT for high tracking efficiency of partially shaded PV module," ***Solar Energy***, vol. 163, pp. 570-580, 2018, doi: https://doi.org/10.1016/j.solener.2017.12.050.

[20] A.I.M. Ali, M.A. Sayed, and E.E.M. Mohamed, "Modified efficient perturb and observe maximum power point tracking technique for grid-tied PV system," ***Electrical Power and Energy Systems***, vol. 99, pp. 192-202, 2018, doi: https://doi.org/10.1016/j.ijepes.2017.12.029

[21] H. Khabou, M. Souissi, and A. Aitouche, "MPPT implementation on boost converter by using T-S fuzzy method," ***Mathematics and Computers in Simulation***, vol. 167, pp. 119-134, 2020, doi: https://doi.org/10.1016/j.matcom.2018.05.010

[22] A. Joseph and J. Kamala, "PV array characteristics analysis under partial shading & modeling of P&O MPPT applied boost convertor using Matlab/Simulink," 2013 International Conference on Energy Efficient Technologies for Sustainability, 2013, pp. 596-601, doi: 10.1109/ICEETS.2013.6533452.

[23] M. Fannakh, M.L. Elhafyani, and S. Zouggar, "Hardware implementation of the fuzzy logic MPPT in an Arduino card using a Simulink support package for PV application," ***IET Renew. Power Gener.***, vol. 13, no. 3, pp. 510-518, 2019, doi: 10.1049/iet-rpg.2018.5667

[24] H. Rezk, and A.M. Eltamaly, "A comprehensive comparison of different MPPT techniques for photovoltaic systems," ***Solar energy***, vol. 112, pp. 1-11, 2015, doi: http://dx.doi.org/10.1016/j.solener.2014.11.010

[25] M. A. Elgendy, B. Zahawi and D. J. Atkinson, "Assessment of the Incremental Conductance Maximum Power Point Tracking Algorithm," in IEEE Transactions on Sustainable Energy, vol. 4, no. 1, pp. 108-117, Jan. 2013, doi: 10.1109/TSTE.2012.2202698.

[26] P.D. Kale, and D.S. Chaudhari, "A review on maximum power point tracking (MPPT) controlling methods for a photovoltaic

system," ***International Journal of Emerging Science and Engineering***, vol. 1, no. 5, pp. 15-19, 2013.

[27] R. Namba, K. Kobayashi, T. Ohkubo, and Y. Kurihara, "Development of PSoC microcontroller based solar energy storage system," ***2011 SICE Annual Conference***, Tokyo, Japan, pp. 718-721.

[28] S. Ozdemir, N. Altin, and I. Sefa, "Fuzzy logic based MPPT controller for high conversion ratio quadratic boost converter," ***International Journal of Hydrogen Energy***, vol. 42, pp. 17748-17759, 2017. doi: http://dx.doi.org/10.1016/j.ijhydene.2017.02.191.

[29] S. A. Mohamed, and M.A.E. Sattar, "A comparative study of P&O and INC maximum power point tracking techniques for grid-connected PV systems," ***SN Applied Sciences***, vol. 2019, pp. 1-174, 2019. doi: https://doi.org/10.1007/s42452-018-0134-4.

[30] A. Azwin, and S. Ahmed, "Induction Motor Speed Control Using Varied Duty Cycle Terminal Voltage via PI Controller," *IOP Conference Series - Materials Science and Engineering*, vol. 341, no. 1, pp. 1–10, 2018, doi: https://doi.org/10.1088/1757-899X/341/1/012013.

[31] B. Wu, Y. Lang, N. Zargari, and S. Kouro, "Wind energy system configurations," in *Power Conversion and Control of Wind Energy Systems,* ed. Hoboken, NJ, USA: John Wiley & Sons Inc., 2011, ch. *5*, pp. *153-171*.

[32] Y. Kim, H. Cha, B. Song and K. Y. Lee, "Design and control of a grid-connected three-phase 3-level NPC inverter for Building Integrated Photovoltaic systems," 2012 IEEE PES Innovative Smart Grid Technologies (ISGT), 2012, pp. 1-7, doi: 10.1109/ISGT.2012.6175663.

[33] A.A. Elbaset, and M.S. Hassan, "Power quality improvement of PV system," in *Design and Power Quality Improvement of Photovoltaic Power System,* ed. Cham, Switzerland: Springer, 2017, ch. *4*, pp. *73-95*.

[34] B. Wu, Y. Lang, N. Zargari, and S. Kouro, "Power converters in wind energy conversion systems," in *Power Conversion and Control of Wind Energy Systems,* ed. Hoboken, NJ, USA: John Wiley & Sons Inc., 2011, ch. *4*, pp. *87-152*.

[35] W. Hong, G. Tao, and H. Wang, "Adaptive control techniques for three-phase grid-connected photovoltaic systems," in *Solar Photovoltaic Power*

Plants – Advanced Control and Optimization Techniques, ed. Singapore: Springer Nature., 2019, ch. *1*, pp. *1-24*.

[36] D.G. Holmes, and T.A. Lipo "Modulation of one inverter phase leg," in *Pulse width modulation for power converter – Principles and practice,* Piscataway, NJ, USA: IEEE Press, 2003, ch. 3, pp. *95-154*.

[37] S.H. Kim "Pulse width modulation inverters," in *Electric Motor Control – DC, AC, and BLDC Motors,* Elsevier, 2017, ch. 7, pp. *265-340*.

[38] B. Mahato, S. Majumdar, and K. C. Jana, "Carrier-based PWM Techniques for Multi-Level Inverters: A Comprehensive Performance Study," *Journal of Science*, vol. 5, no. 3, pp. 101-111, 2018

3. ANALYSIS AND RESULTS

This section is divided into three sub-sections. The first sub-section describes the data collection and analysis methodology employed for wind and solar data. The second sub-section depicts and describes the final power output and other vital parameters resulting from the designed PV-wind hybrid system. Finally, the third consists of cost and payback period calculations for the designed PV-wind hybrid system which sends power to utility grid.

Data analysis

Monthly wind and solar data for Valentine, Nebraska (coordinates – 42°54'33.7"N 100°32'43.2"W) was utilized to design the PV-wind hybrid renewable energy system. Hourly wind data was available at 10m height and it was recalculated for a height of 30m using equation 3.1 [1]. The height of 30m was chosen based on the literature, which specifies that the average installation height of 5-12kW wind turbines is 18-36m [2].

$$v_{30} = v_{10}\left(\frac{h_{30}}{h_{10}}\right)^{\alpha} \tag{3.1}$$

where

$v_{30,}\ v_{10}$ are the speeds of wind flow in m/sec at the heights of $h_{30}\ (30m)$ and $h_{10}\ (10m)$;

α is the shift factor (if the value is unknown, it is assumed: α = 1/7).

Table 3.1 shows the average hourly wind speed data for a 30m height calculated for each month for the chosen location. The calculated hourly data was then converted into average monthly wind speed which is shown in figure 3.1. As depicted, the average wind speeds in Valentine, Nebraska are lower from May to October as compared to the rest of the year with lowest being 4.8 m/sec in July. The highest average wind speed of 7.7 m/sec was observed in the month of February.

Similarly, the hourly solar irradiation data was collected for Valentine, Nebraska and summarized for each month as shown in table 3.2. As the data depicts, the irradiation from 9pm to 6am was significantly low and therefore was neglected for the analysis since these irradiation levels would not generate any usable power. The average monthly irradiation data for the time between 7am to 8pm is shown in figure 3.2. As expected, the data shows that that the average monthly solar radiation was lower

between October and February as compared to rest of the year. The maximum level of irradiance of 460.2 W/m^2 was observed in the month of July.

Table 3.1. Average hourly wind data for each month

Time of day	**Month**											
	Jan	Feb	Mar	Apr	May	June	July	Aug	Sept	Oct	Nov	Dec
0100	6.2	6.9	6.6	6.0	5.1	4.8	4.4	4.7	5.6	5.2	6.3	6.4
0200	6.3	6.8	6.4	6.2	5.0	4.9	4.5	5.0	5.7	5.1	6.3	6.3
0300	6.4	7.1	6.1	6.2	5.3	5.0	4.6	4.7	5.6	5.3	6.2	6.1
0400	6.3	7.0	6.0	6.4	4.9	4.6	4.6	4.6	5.5	5.4	6.3	6.2
0500	6.7	7.0	6.2	6.6	4.8	4.7	4.3	5.0	5.3	5.5	6.4	6.4
0600	6.5	7.0	6.4	6.5	4.9	4.8	4.4	4.6	5.2	5.7	6.6	6.3
0700	6.6	7.1	6.3	6.6	5.1	5.6	4.2	4.5	5.4	6.0	6.3	6.4
0800	6.6	7.1	6.4	7.3	5.7	5.7	4.1	4.5	5.4	5.9	6.4	6.6
0900	6.3	7.4	6.7	8.0	6.5	6.0	4.7	4.8	6.2	6.1	6.7	6.3
1000	6.4	7.7	7.1	8.3	6.9	6.1	5.2	5.1	6.9	6.4	6.8	6.2
1100	6.7	8.5	7.2	8.3	6.8	6.2	5.5	5.0	6.8	6.6	7.1	6.8
1200	7.0	9.4	7.5	8.2	6.9	6.5	5.4	5.3	7.2	6.4	7.4	7.4
1300	7.4	9.7	7.8	8.2	7.0	6.6	5.6	5.6	7.4	6.8	7.7	7.7
1400	7.2	9.7	8.0	8.1	7.1	6.8	5.6	5.6	7.5	6.5	7.5	7.8
1500	7.6	9.8	8.1	7.9	7.0	7.1	5.5	6.1	7.2	6.6	7.5	8.0
1600	7.4	9.7	8.2	8.0	6.7	6.8	5.3	6.6	7.3	6.7	7.4	7.8
1700	7.0	9.0	8.1	8.2	6.7	7.0	5.4	6.6	7.2	6.5	6.8	6.7
1800	6.5	7.4	7.8	8.1	7.2	6.9	5.0	6.5	6.7	5.8	6.7	6.0
1900	6.1	6.7	6.8	7.4	6.9	6.1	4.9	5.9	5.3	5.2	6.7	5.8
2000	5.7	6.3	6.7	6.2	5.3	5.8	4.4	4.7	5.1	5.1	6.7	6.1
2100	5.8	6.4	7.1	5.4	4.5	5.9	4.7	4.4	5.4	5.4	6.5	6.1
2200	5.7	6.5	7.5	5.2	4.7	6.1	4.8	4.7	5.5	5.3	6.8	6.4
2300	5.8	6.9	7.1	5.3	4.8	5.1	4.5	5.0	5.6	5.0	6.6	6.5
2400	6.1	6.8	7.0	5.6	5.3	5.1	4.4	4.7	5.7	5.3	6.6	6.3

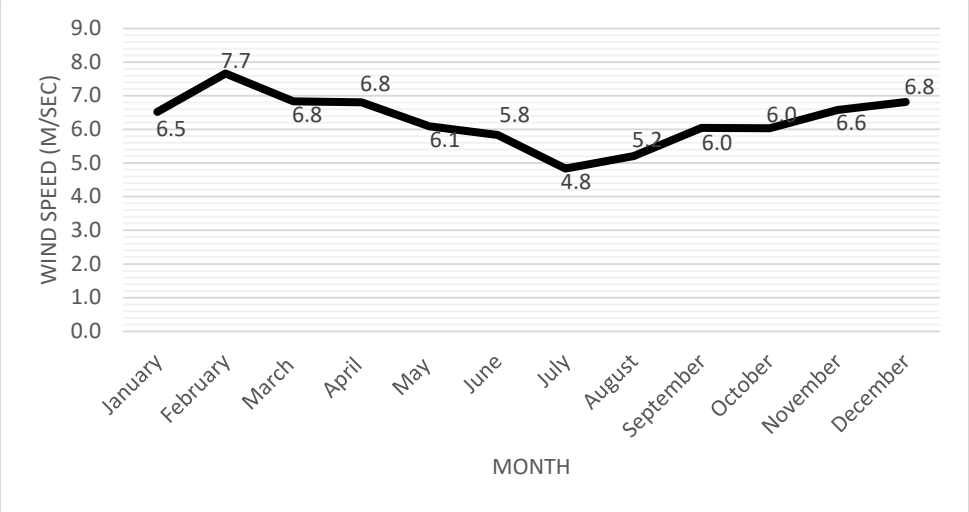

Figure 3.1. Average monthly wind speed for Valentine, Nebraska.

Table 3.2. Average hourly irradiance data for each month

Time of day	**Month**											
	Jan	Feb	Mar	Apr	May	June	July	Aug	Sept	Oct	Nov	Dec
0100	1.4	1.4	1.4	0.0	0.0	0.0	0.0	0.0	0.0	2.6	3.0	2.1
0200	1.4	1.4	1.4	0.0	0.0	0.0	0.0	0.0	0.0	1.1	3.0	2.2
0300	1.4	1.4	1.4	0.0	0.0	0.0	0.0	0.0	0.0	1.1	3.3	2.2
0400	1.4	1.4	1.4	0.0	0.0	0.0	0.0	0.0	0.0	1.1	3.0	2.2
0500	1.4	1.4	1.4	0.0	0.0	0.0	0.0	0.0	0.0	1.1	3.0	2.2
0600	1.4	1.4	1.4	0.9	9.8	19.7	7.0	1.9	0.0	1.1	3.2	2.2
0700	1.4	1.4	2.3	35.6	88.1	106.5	63.7	43.4	15.1	2.3	3.3	2.2
0800	1.4	4.3	44.8	144.2	213.7	233.7	186.6	162.4	119.0	30.4	9.0	4.9
0900	11.6	71.4	173.0	276.9	340.9	382.5	341.0	325.7	269.5	133.9	57.2	22.8
1000	91.3	199.2	304.2	432.3	470.0	519.6	477.6	466.9	415.7	249.9	154.6	119.8
1100	194.2	320.4	418.0	564.0	594.6	641.2	629.6	598.1	554.6	341.5	244.2	237.0
1200	279.6	419.8	510.1	649.8	677.1	680.3	718.6	746.5	662.6	399.5	307.0	322.1
1300	324.0	470.3	577.2	675.0	722.2	665.6	775.4	763.6	712.7	420.4	331.2	375.0
1400	321.5	476.9	571.9	675.3	703.4	675.1	762.1	745.7	671.6	397.2	311.2	365.6
1500	286.0	459.1	522.2	600.0	716.7	625.8	695.3	689.2	618.0	335.8	260.8	306.1
1600	193.7	357.0	440.2	484.4	624.6	539.1	608.5	583.3	510.5	249.4	178.4	203.9
1700	98.7	226.5	304.0	381.5	471.2	456.8	509.0	452.5	349.6	149.7	78.4	87.4
1800	23.4	75.2	155.8	240.4	320.0	319.0	361.6	295.2	184.4	26.2	10.2	8.7
1900	1.5	5.1	36.2	103.2	170.3	175.2	223.9	136.4	20.0	1.3	3.0	2.1
2000	1.4	1.4	1.8	0.1	20.3	71.8	90.2	0.2	0.0	1.1	3.2	2.2
2100	1.4	1.4	1.4	0.0	0.0	0.0	0.0	0.0	0.0	1.3	2.8	3.0
2200	1.4	1.4	1.4	0.0	0.0	0.0	0.0	0.0	0.0	1.4	3.3	4.2
2300	1.4	1.4	1.4	0.0	0.0	0.0	0.0	0.0	0.0	1.4	2.7	3.5
2400	1.4	1.4	1.4	0.0	0.0	0.0	0.0	0.0	0.0	1.7	2.8	2.6

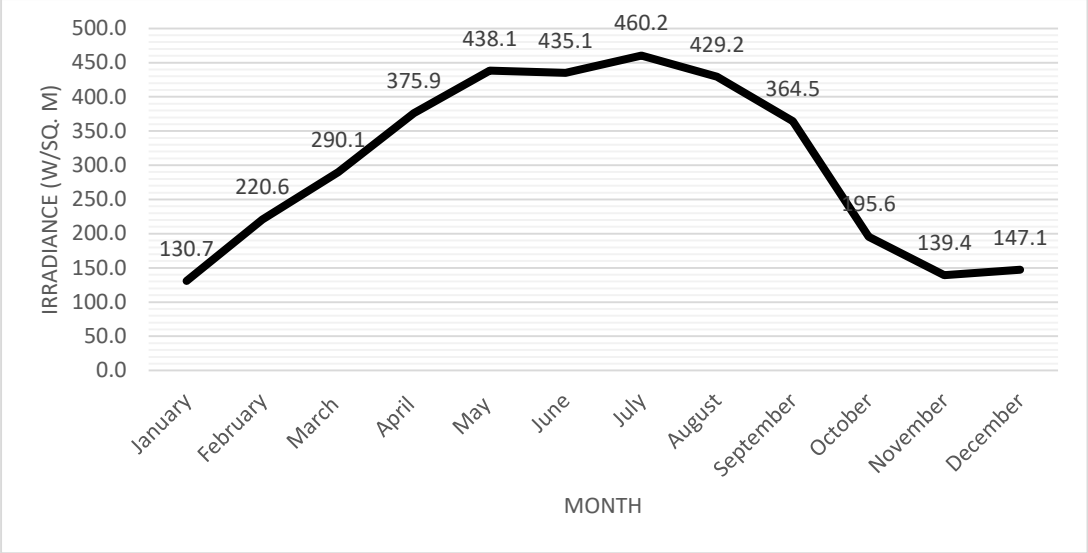

Figure 3.2. Average monthly irradiance data for Valentine, Nebraska.

As can be inferred from the solar irradiance and wind speed data for the chosen location, February had the maximum average wind speed but low average irradiance levels. On the other hand, July had maximum monthly solar radiation and minimum wind speeds on an average. Considering that the months of February and July encompass the worst- and best-case scenarios for solar and wind data, the results presented in the next sub-section will focus on these two months.

Results

The data shown in the previous section was utilized to simulate the grid-connected 12kW hybrid PV-wind renewable energy setup for power generation designed for small-scale applications. The system simulated in the present investigation consisted of a combination of 12kW wind turbine and a 12.8kW rated solar array. A summarized list of parameters of main components used to design the proposed system is listed below:

A. Wind turbine section:

i) Wind turbine – 12kW at rated wind speed of 14m/sec

ii) DC-DC boost converter – L=1.875x10^{-5} H; C=1x10^{-3} F

B. PV module section:

iii) PV array – 12.8kW at rated solar irradiation of 1000 W/m^2; 6 series-connected modules in 10 parallel strings

iv) DC-DC boost converter – L=8.2x10^{-3} H; C=1x10^{-3} F

v) MPPT – P&O algorithm

C. Inverter and filter parameters:

vi) Inverter – Voltage source inverter

vii) Controller parameters – Proportional, P = 0.0033; Integral, I = 1.1081

viii) Filter – L-filter; L = 4.1125×10^{-4} H

As specified in the model description, the DC-DC boost converter was designed such that it converted the variable input voltage from wind turbine to a constant 500V output. Similarly, the PV array was connected to a separate DC-DC boost converter in order to get the 500V constant output. The 500V output voltage from the DC-DC boost converters for the designed system is referred to as V_{bus} and shown in figure 3.3. The result shows that the designed system was able to convert the variable input voltages from the wind turbine and solar array to a stable and constant value of 500V.

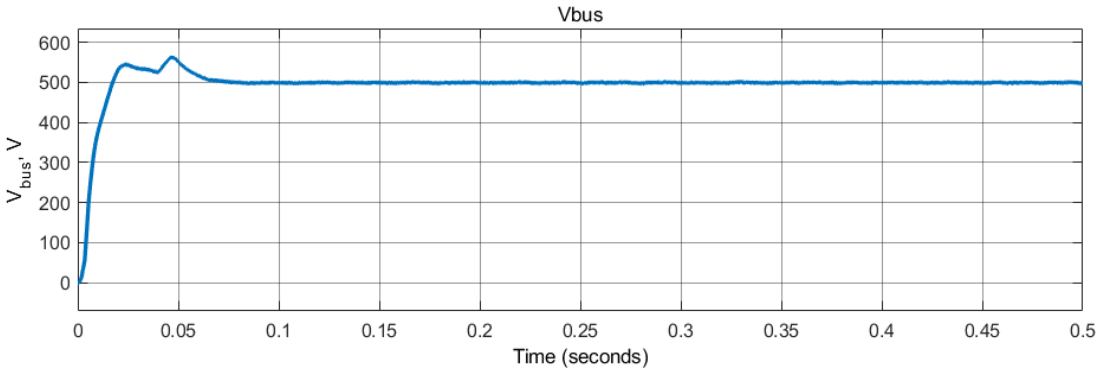

Figure 3.3. Output voltage from DC-DC boost converters.

The output power of the designed HRES was calculated for the rated wind speed of 14m/sec and rated solar panel irradiance of $1000 W/m^2$. The result, depicted in figure 3.4, shows that at rated wind speed and irradiance levels, the designed system yields the required 12kW power to satisfy the load requirement. As mentioned in section 3.1, the wind speed data and solar irradiance data for February and July were focused on and the output power from the designed system were simulated for these two months. The results of the same are shown in figures 3.5 and 3.6. It was observed that for the month of February, the maximum power out from wind turbine was 3.5kW, from PV was 6.1kW and from the complete hybrid PV-wind system was 9.4kW. The maximum power was generated between 1pm and 3pm with both average wind speed and average irradiance being the highest at this time of the day.

Since the average wind speed in July was 4.8m/s which was lower than in February and considerably lower than the rated speed of 12m/s, therefore the contribution of output power from wind turbine was drastically lower as compared to

that of PV. As depicted in figure 3.6, the maximum power out from wind turbine was approximately 50W, from PV array was 9.9kW and from the complete hybrid PV-wind system was 9.95kW. The maximum power output was observed between 1pm and 2pm.

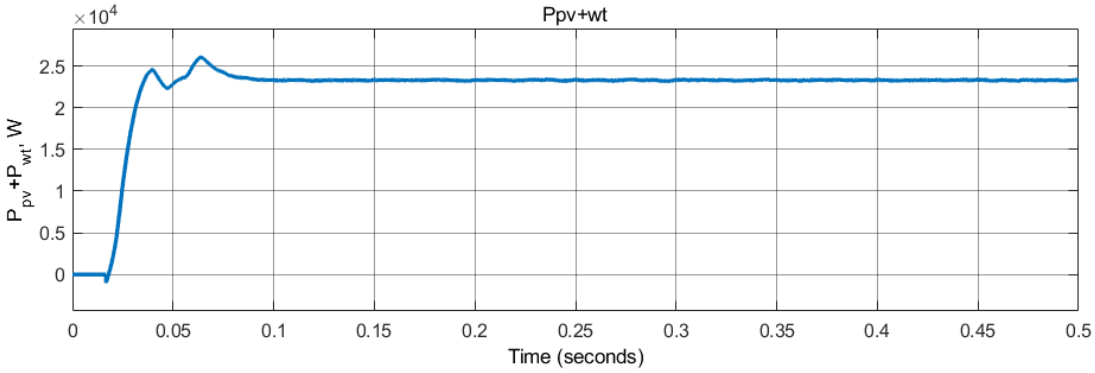

Figure 3.4. Hybrid system power output

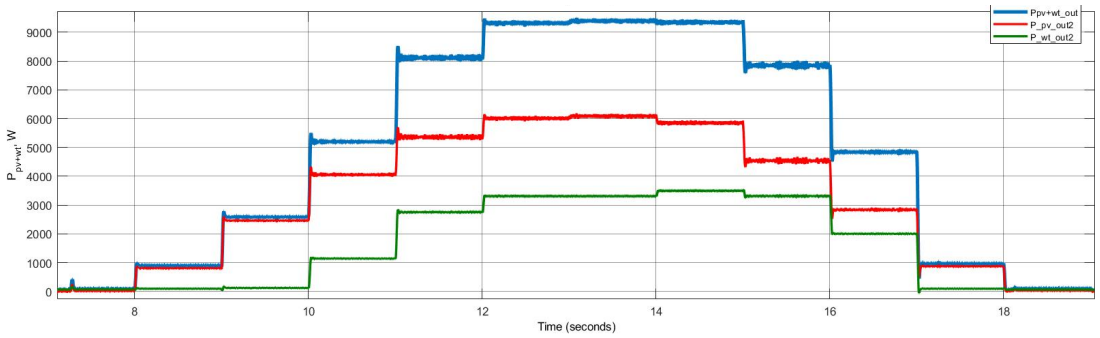

Figure 3.5. PV, wind and hybrid output power for February

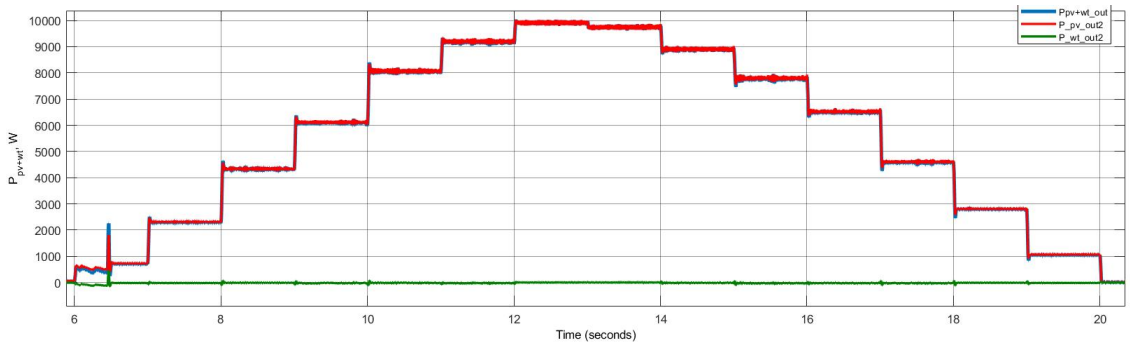

Figure 3.6. PV, wind and hybrid output power for July

Cost Analysis

Cost of PV and wind energy systems has considerably been reduced over the last decade due to technological advancements, economies of scale, and improved and interconnected global supply chain [3]. According to International Renewable Energy Agency (IRENA), levelized cost of electricity of wind energy systems reduced by 9% and that of utility scale PV systems fell by 7% [3]. This analysis takes into consideration

the average market value of major sub-components of the designed hybrid PV-wind system based on available literature and surveys conducted by various private and public organizations.

Wind turbine cost calculation: Costs related to wind turbine can be primarily categorized into capital cost and variable cost [4]. Capital cost comprises of the cost of wind turbine including the cost of blades, transformers, transportation and installation. It also includes construction related costs, cables, connections and licensing costs. Depending on the installation location and type of wind turbine, the capital cost can be as high as 80% of the total wind turbine cost project [4]. The variable cost mainly constitutes operation and maintenance costs, land rentals, insurance, taxes, and management costs. The costs specified in this analysis will vary on depending on multiple factors and are not meant to be exact market prices. The capital and variable costs depicted below are average prices based on literature.

(i) Capital cost: Average cost of wind turbine and other constituents on capital cost is $2700/kW. Therefore, for a 12kW system, total capital cost would approximate be 12x2700 = $32,400.

(ii) Variable cost: Considering maintenance requirement every 6 months, the estimated cost including insurance is 1.5 cent per kWh produced over lifetime of wind turbine.

PV system cost calculation: The US national average of a solar panel system is $2.66/W and for the state of Nebraska the cost is significantly higher, i.e. $2.83/W. The size of the PV system is the primary factor influencing its cost and based on the available data, 1kW solar system costs $2830 on an average. Therefore, for the 12.8 kW system under consideration, the total cost of the system would be 12.8x2830 = $36,224.

Inverter cost: The peak power delivered by the hybrid PV-system depends on the size of the inverter implemented in the system. Based on surveys, the inverter cost of the system is $0.28/W [5]. Therefore, if the load draws complete 12kW peak power, then the inverter cost would come out to be 280x12 = $3360. Summary of the cost calculations is depicted in table 3.3.

Table 3.3. Cost summary of the proposed system

Sub-system	**Cost ($)**
Wind turbine system	$32,400
PV system	$36,224
Inverter	$3,360

Based on table 3.3, the total upfront cost of the PV panels, wind turbine, inverter and batteries is: $32,400 + $36,224 + $3,360 = $71,984.

Payback Period: In order to calculate the time required to get the return on investment, the monthly kWh produced by the hybrid system was calculated for Valentine, Nebraska as shown in table 3.4. Based on the solar irradiation and wind speed data for Valentine, the annual energy produced by the hybrid system come out to be approximately 19716 kWh. The average cost of commercial electricity in Valentine, Nebraska is $0.1007/kWh. The annual cost to consumer, in order to consume 19716 kWh was calculated to be $1985.42. Therefore, the payback period for the hybrid system can be calculated as:

$$Payback\ Period = \frac{Cost\ of\ hybrid\ system}{Annual\ energy\ cost\ to\ consumer} \tag{3.2}$$

$$= \frac{\$71984}{\$1985.42} = 36.3$$

The payback period for implementing the PV-wind hybrid system in Valentine, Nebraska was calculated to be approximately 36 years which is higher than the estimated product lifetime of 15-25 years. Low wind speed and solar irradiation in this region led to considerably lower availability of power available for consumption from the hybrid system, therefore, leading to a higher payback period. Hypothetically, if the system would run at its rated power of 12 kW, then 105120 kWh electricity would be available for consumption and assuming 100% consumption, the payback period would be slightly less than seven years.

Furthermore, for the selected region, the PV system contributes most of the energy generated by the system due to very low wind speeds throughout the major portion of the year. As depicted in tables 3.4 and 3.5, the solar system generates more than 97% of the total power. Hence for this region, it could be inferred that a PV-based

renewable energy system would be financially more viable. This was also confirmed by the payback period calculation for a PV-system which resulted in a payback period of approximately 20 years as compared to 36 years with a PV-wind hybrid system.

Table 3.4. Payback period calculation for PV-wind hybrid system

PV-Wind Hybrid system				
	Valentine, Nebraska		Potential data	
Month	Average per hour per day (kW)	Total energy per month (kWh)	Average per hour per day (kW)	Total energy per month (kWh)
Jan	0.96	714.24	12	8928
Feb	1.68	1128.96	12	8064
Mar	2.18	1621.92	12	8928
Apr	2.83	2037.6	12	8640
May	3.28	2440.32	12	8928
Jun	3.26	2347.2	12	8640
Jul	3.39	2522.16	12	8928
Aug	3.14	2336.16	12	8928
Sep	2.7	1944	12	8640
Oct	1.42	1056.48	12	8928
Nov	1.04	748.8	12	8640
Dec	1.1	818.4	12	8928
TOTAL (per year)		19716.24		105120
Total payment per year (USD)		1985.43		10585.58
Payback period (Years)		36.3		6.80

Table 3.5. Payback period calculation for PV system for Valentine, NE

	Valentine, Nebraska	
Month	Average per hour per day (kW)	Total energy per month (kWh)
Jan	0.9	669.6
Feb	1.56	1048.32
Mar	2.1	1562.4
Apr	2.75	1980
May	3.22	2395.68
Jun	3.2	2304
Jul	3.39	2522.16
Aug	3.14	2336.16
Sep	2.66	1915.2
Oct	1.38	1026.72
Nov	0.98	705.6
Dec	1.04	773.76
TOTAL (per year)		19239.6
Total payment per year (USD)		1937.43
Payback period (Years)		20.43

Final output power from the hybrid system as well from the PV and wind-based renewable energy systems for Valentine is shown in figure 3.7.

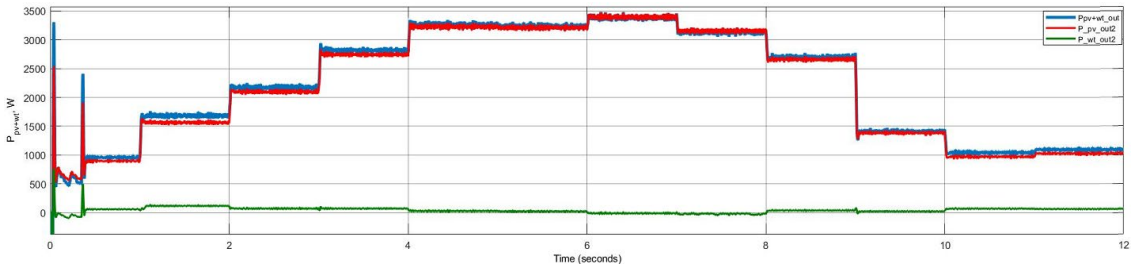

Figure 3.7. PV, wind and hybrid output power in Valentine, NE

REFERENCES

[1] S. Heier, “Wind energy conversion systems,” in *Grid Integration of Wind Energy – Onshore and Offshore Conversion Systems, 3rd* ed. Wiesbaden, Germany: Vieweg+Teubner (in German), 2009, ch. *2*, pp. *31-116*.

[2] R.N. Clark, “Needs evaluation – Determining power need to meet the owner’s request,” in *Small wind planning and building successful installations, 1st* ed. Waltham, MA, USA: Academic Press, 2013, ch. *2*, pp. *29-37*.

[3] International Renewable Energy Agency, “Renewable power generation costs in 2020,” 2021. [Online]. Available: Renewable Power Generation Costs 2020 (irena.org)

[4] M.I. Blanco, "The economics of wind energy, "*Renewable and Sustainable Energy Reviews*, vol. 13, pp. 1372-1382, 2009, doi:10.1016/j.rser.2008.09.004

[5] “Solar Panel Cost Nebraska: Prices and Data.” solarreviews.com. Solar Panel Cost Nebraska: Local prices & online estimator (solarreviews.com) (accessed June 19, 2022)

4. CONCLUSION AND FUTURE WORK

This research proposed a 12kW PV-wind hybrid renewable energy system model. The model consisted of a 12.8kW solar array and a 12kW wind turbine connected to the grid with phase-to-phase rms voltage value of 208V and a frequency of 60Hz. The PV system was connected to a voltage source inverter through a dc-dc boost converter. Maximum power point tracking algorithm was used to track and maintain the maximum available power out of the PV system to be provided as input to the boost converter. Maximum power was obtained from the PV system irrespective of weather conditions due to implementation of MPPT. The wind turbine was connected to a common dc bus of 500V through ac-dc rectifier and dc-dc boost converter which was operated in continuous conduction mode with pre-calculated duty cycle. Since MPPT was not implemented due to cost and size constraint, there was some reduction in output power from wind turbine. The hybrid system was connected to the grid through a voltage source inverter and an L-filter. Average model of voltage source inverter in dq0 coordinates was derived for system control modeling. Open-loop transfer function of the control system was derived in order to obtain the proportional and integral parameters of PI controller. Decoupling terms were implemented to eliminate the effect of other coordinates while calculating the transfer functions. All sub-components of the proposed model were designed to design a well-functioning system which meets the required parameters.

Solar and wind data from Valentine, Nebraska were then utilized as inputs to the proposed hybrid model, and output power and voltage characteristics were obtained for this region such that we obtain maximum power that can be generated by the system. Furthermore, a cost analysis was done to calculate the payback period of the proposed system for the chosen region. It was observed that due to low wind speed and solar irradiation, the output power was significantly lower than the rated power for which the system is designed for. Due to this, the payback period also turned out to be very high (approximately 36 years), whereas if operated at rated parameters, the payback period reduces considerably to approximately 7 years. It was also observed that for the selected region, the PV system was responsible for generating more than 97% of the total power and therefore, it would be financially viable to use a PV-based renewable energy system.

Further research and analysis on the proposed hybrid system must be done in order to gain deeper understanding and to look into various improvements that might be able to create a more efficient and cost-effective PV-wind hybrid renewable energy system. Some of the areas of interest for future research could be:

1. Implementing an energy storage system or a battery module to store and discharge energy based on available power supply and load demand. When connected to such a system, the battery is in charging state when the total power generated by the system is higher than the energy demand. Alternatively, when the load demand is higher than the energy generated, the battery switches to discharging state. A combination of a battery module with a bidirectional buck-boost converter could be implemented used to supply the back-up power from the battery to load when power generated by solar and wind energy systems is insufficient to meet the system requirement, and to transfer power to the battery module when load requirement is less than the energy generated by HRES [1].
2. As shown in figure 2.33, there are multiple types of PWM techniques, with each one having its own set of advantages and disadvantages. The effect of implementing different PWM methodologies such as the space vector PWM or the third harmonic injection PWM could be studied in order to reduce the switching losses.
3. The model must be analyzed in different regions, especially in the ones with higher wind speeds and solar irradiation and the payback period for the same must be calculated in order to get a better understating of the cost-effectiveness of the model and to figure out the minimum environmental conditions favorable to make the proposed system financially viable.
4. The proposed system must be manufactured and tested in lab setting as well as installed at multiple locations and measured output parameters of the actual system must be compared to the model simulated in Simulink. This is vital to get a clarity on the accuracy of the Simulink model with respect to real-world conditions and would help in creating more accurate models in future.

REFERENCES

[1] R.J. Wai and R.Y. Duan, "High-Efficiency Bidirectional Converter for Power Sources With Great Voltage Diversity," in IEEE Transactions on Power Electronics, vol. 22, no. 5, pp. 1986-1996, Sept. 2007, doi: 10.1109/TPEL.2007.904167.